J. Fluid Mech. (2021), *vol*. 912, A7, doi:10.1017/jfm.2020.989

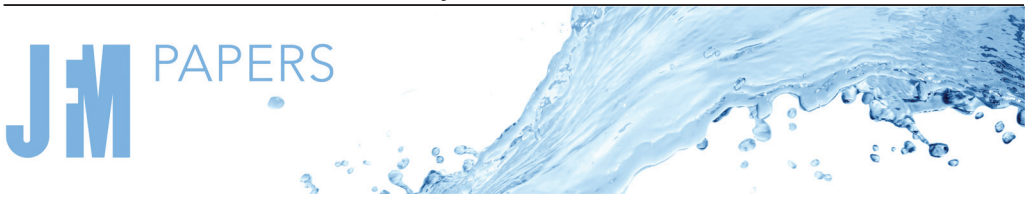

Characterization of the shear layer in separated shock/turbulent boundary layer interactions

Clara M. Helm[1], **M. Pino Martín**[1,†] **and Owen J.H. Williams**[2]

[1]Department of Aerospace Engineering, University of Maryland, College Park, MD 20742, USA

[2]William E. Boeing Department of Aeronautics and Astronautics, University of Washington, Seattle, WA 98195, USA

(Received 22 November 2019; revised 2 November 2020; accepted 3 November 2020)

A thorough characterization of the shear layer that exists in large eddy simulation data of three separated, compression ramp-generated shock/turbulent boundary layer interactions is presented. Free stream Mach numbers ahead of the separation shock are 2.9, 7.2 and 9.1. The shear layers produced by the separation in these flows have convective Mach numbers of 1.0, 1.9 and 2.0, respectively. It is found that the separation shear layers share many properties associated with canonical compressible mixing layers. A region of approximate similarity is found in each where it is possible to collapse the mean flow profiles into nearly a single similarity profile. Large mixing-layer-like vortical rollers are found in the shear layers and these are shown to become increasingly three-dimensional with increasing convective Mach number. The relation between the peak turbulence stress and the spreading rate was found to be consistent with mixing layer data and mixing layer theory derived from dimensional analysis. Turbulent kinetic energy and Reynolds stress budget analysis revealed that, although the streamwise turbulence production is greater than the canonical mixing layer, the transfer of turbulence energy by the pressure–strain terms and the energy drain by viscosity terms both show similar behaviour to mixing layer data at matching convective Mach number. As a result, the spreading rate and turbulence anisotropy decrease with increasing M_c. These conclusions are aided by an accurate and direct measurement of the vortex convection velocity determined from enhanced two-point correlations in the shear flow. The usefulness of studying the shock/turbulent boundary layer flow in this manner is emphasized.

Key words: compressible turbulence, shear layer turbulence, shock waves

1. Introduction

The free shear layer is one of the most fundamental shear flows for the study of turbulence. Unlike wall-bounded shear layers, the mixing layer develops with only one length scale.

† Email address for correspondence: mpmartin@umd.edu

The canonical mixing layer therefore affords a simple yet essential configuration for the study of compressible turbulence. A firm grasp of the fundamental physics of compressible turbulence in shear flow is of paramount importance for the advancement of hypersonic flight technology, supersonic combustion and the development of robust practical simulation tools for such engineering design efforts.

Despite its conceptual simplicity, the compressible mixing layer exhibits certain properties that are difficult to explain physically. One of its most documented features is a significant decrease in spreading rate with increasing compressibility. This property is noted in research articles as early as the 1950s from experimental observation (Korst & Tripp 1957; Channapragada 1963) and from linear stability prediction of the stabilizing effects of increasing Mach number on a vortex sheet (Lin 1953; Pai 1955; Miles 1959). By the 1970s, consensus among scientists resulted in the well known 'Langley curve' (Birch & Eggers 1972; Kline, Cantwell & Lilley 1980). The Langley curve is generally plotted as normalized spreading rate versus the convective Mach number M_c, a metric for compressibility proposed by several authors (Bogdanoff 1983; Chinzei *et al.* 1986; Papamoscho & Roshko 1988). Early research also revealed that the reduction in spreading rate is accompanied by a reduction in fluid entrainment, turbulence mixing and turbulence stresses (Ikawa & Kubota 1975; Elliott & Samimy 1990; Goebel & Dutton 1991). Many significant research contributions advancing our physical understanding of these phenomena have since been put forward as outlined in several review articles (Dimotakis 1991; Lele 1994; Smits & Dussauge 2006; Gatski & Bonnet 2013). In spite of the large volume of research, precise scaling laws and robust models for simulation are still lacking.

Several factors make identification of exact scaling dependencies difficult. Significant spread exists in the data partly due to limitations of measurement techniques, but also due to an acute sensitivity of the mixing layer to initial and boundary conditions. This sensitivity is problematic in both experiment and computation and can produce large variations in the spreading rate and turbulence stresses. Disturbances in the free stream, conditions of the boundary layer, experimental facility acoustics, splitter plate vibration, and test section confinement can all contribute to scatter in the data (Smits & Dussauge 2006; Gatski & Bonnet 2013). In the classic relation of Papamoscho & Roshko (1988) $\delta' = \delta'_{inc}\phi(M_c)$, determination of the scaling function $\phi(M_c)$ is compromised by significant scatter in both the compressible spreading rate δ' and the incompressible spreading rate δ'_{inc}. Dimotakis (1991) reported as much as a 30 % variation in incompressible spreading rate data due to experimental inconsistencies. Smits & Dussauge (2006) estimated as much as a 50 % variation in the compressible data measurements. A number of attempts have been made to correct for the discrepancies in the data (Slessor, Zhuang & Dimotakis 2000; Aupoix 2004; Aupoix & Bézard 2006; Barone, Oberkampf & Blottner 2006) with some success, however, large spread in the data still remains. Similarly for turbulence quantities, scatter has prevented a consensus on the trends caused by increasing compressibility. For example, many studies indicate that the peak normal stress in both the streamwise ($\overline{u'^2}$) and cross-stream ($\overline{w'^2}$) directions steadily decrease with increasing M_c. This resulted in the turbulence shear stress ($\overline{u'w'}$) and anisotropy ($\overline{u'^2}/\overline{w'^2}$) remaining relatively constant (Samimy & Elliott 1990; Barre, Quine & Dussauge 1994; Debisschop, Chambres & Bonnet 1994; Pantano & Sarkar 2002). Still, several other studies (Goebel & Dutton 1991; Gruber, Messersmith & Dutton 1993; Freund, Lele & Moin 2000) found that for increasing M_c, $\overline{u'^2}$ is constant and only $\overline{w'^2}$ decreases causing the shear stress to decrease and anisotropy to increase. The overall scatter is of the order of the reported trends, as can be seen in the data compilations in Smits & Dussauge (2006) and also in the more recent data compilations of Barre & Bonnet (2015).

The sensitivity of the mixing layer stems from the complex dynamics of the large-scale vortices produced by the Kelvin–Helmholtz instability. These large-scale mixing layer eddies undergo significant changes with increasing Mach number and have been found to play a dominant role in establishing both the spreading rate and turbulence levels. It has been observed in many studies that the structure of the mixing layer becomes increasingly three-dimensional (3-D) and less coherent with increasing compressibility. This has been shown, for example, with two-point correlations in experimental data (Samimy, Reeder & Elliott 1992), in experimental flow visualizations (Clemens & Mungal 1992, 1995; Rossmann, Mungal & Hanson 2002) and flow visualizations in numerical simulations (Sandham & Reynolds 1991; Day, Reynolds & Mansour 1998; Freund *et al.* 2000; Kourta & Sauvage 2002). Increasing strength of an oblique unstable wave with convective Mach number was also predicted by inviscid stability theory (Sandham & Reynolds 1990, 1991). Further complexity arises when the motion of the large vortices becomes supersonic relative to one or both of the external flows causing shocklets to appear. Shocklets have been observed both experimentally (Papamoschou 1995; Rossmann *et al.* 2002) and in simulations (Lele 1989; Freund *et al.* 2000; Kourta & Sauvage 2002) and typically occur at high convective Mach numbers. These shocklets can affect the turbulence dilatation, dissipation and pressure fields (Smits & Dussauge 2006).

A key parameter for the characterization of the compressible mixing layer is the convection velocity of the Kelvin–Helmholtz vortices in relation to one or both of the free stream velocities. Under the assumption that the mixing layer eddies convect at a constant velocity, are non-dispersive, and the streamlines are isentropic, Papamoscho & Roshko (1988) conducted a theoretical analysis to derive the convective Mach number $M_c = \Delta U/(a_1 + a_2)$ which is the velocity difference across the layer ΔU divided by the average of the sound speed a in the two streams. Despite the limitations imposed by the derivation assumptions, M_c is still the most used Mach number in the study of compressible mixing layers. Freund *et al.* (2000) showed in their direct numerical simulations (DNS) of an annular mixing layer that, with increasing M_c, the cross-stream correlation length decreases in relation to the layer thickness. This indicates that the large-scale eddies do not span the width of the layer at elevated Mach number. The same authors also showed that the peak turbulence stress in their simulation data scaled with the cross-stream correlation length and not the layer thickness. These results were confirmed by Pantano & Sarkar (2002) who demonstrated that the pressure–strain rate correlation in their DNS scaled best with the so-called gradient Mach number. The gradient Mach number M_g is by definition the acoustic time scale divided by the flow distortion time scale and is related to the velocity difference across a large-scale structure. This is in contrast to M_c which is based on the velocity difference across the entire layer. The results of Freund *et al.* (2000) and Pantano & Sarkar (2002) are both consistent with the previous work by Vreman, Sandham & Luo (1996) who used a theoretical model of a sonic eddy, a concept first introduced by Breidenthal (1992), to explain an observed decrease in pressure fluctuations with increasing Mach number. Detailed turbulence statistics afforded by high-fidelity numerical simulations enabled these authors (Vreman *et al.* 1996; Freund *et al.* 2000; Pantano & Sarkar 2002) to reveal that a decrease in the pressure–strain rate correlation is directly responsible for the decrease in spreading rate with increasing Mach number. These results point to the importance of the structural changes of the large-scale mixing layer eddies in dictating both the spreading rate and the turbulence stresses.

One factor limiting our ability to translate these observations into precise scaling laws is that the parameter space has by no means been exhausted. Particularly lacking in the research are mixing layers of high convective Mach number ($M_c > 1$), especially in the way of turbulence statistics. Aside from the notable work by Pantano & Sarkar (2002),

the effects of density gradient on the compressible mixing layer dynamics and their distinction from purely compressibility effects has not yet been thoroughly explored. The effect of velocity ratio also has not been fully investigated. The majority of mixing layer data are either of a single stream or two coflowing streams. There is evidence, however, that the vortex dynamics are fundamentally different for the counter-current configuration compared with the much more widely studied coflowing configuration. Flow visualizations of the axisymmetric jet of Strykowski, Krothapalli & Jendoubi (1996) demonstrate that counter-flow shear layers can produce larger and more coherent structures than are discernible in single-stream jets at similar conditions. Linear stability analysis of both compressible and incompressible mixing layers shows the unstable mode can transition from a convectively unstable to an absolutely unstable mode under certain conditions of reverse flow strength (Huerre & Monkewitz 1985; Pavithran & Redekopp 1989; Jackson & Grosch 1990). Considering these changes in the nature of the instability, a question that may be asked is whether the relations between spreading rate and turbulence statistics observed in coflowing compressible mixing layers still hold true. Another configuration of practical interest of which there is very little data available is the mixing layer subjected to a streamwise pressure gradient.

A compressible separation shear layer forms in strong shock/turbulent boundary layer interactions (STBLI). A well known characteristic of separated STBLI is the occurrence of a low-frequency unsteadiness in the shock foot and separation bubble (among many references, see for example Dussauge, Dupont & Debiève (2006) and Wu & Martín (2008)). Many attempts have been made to discover the origins of this unsteadiness, but of particular interest to the current discussion is the work of Piponniau *et al.* (2009) who used scaling arguments to explain the order of magnitude difference between low-frequency motions observed in STBLI and those observed in incompressible separation bubbles. In the derivation of their model, they equated the separation shear layer in their Mach 2.3 reflected shock STBLI to a canonical mixing layer and cited the Mach number dependent reduction in the spreading rate of the compressible mixing layer as the primary cause of the frequency difference. Recently, Dupont, Piponniau & Dussauge (2019) published a follow-up article to that of Piponniau *et al.* with the intention of verifying the assumptions that were made of the STBLI shear layer properties. Although decidedly not a canonical mixing layer, interestingly, Dupont *et al.* showed that the STBLI shear layer does in fact share many of the same properties. For example, they were able to collapse profiles of the mean velocity and turbulence stresses onto an approximate similarity profile by defining an appropriate, linearly varying, shear layer coordinate system. They also demonstrated that the spreading rate of the separation shear layer was consistent with the level of compressibility as determined by the convective Mach number and the measured rate of entrainment. Turbulence scaling properties of shear stress-to-spreading rate and also turbulence anisotropy-to-convective Mach number were also found to be in good agreement with mixing layer dimensional analysis. In light of these results, it would seem that the separation shear layer in STBLI flows could potentially provide significant insight into the mixing layer problem, or, at the very least, help expand the currently available parameter space.

We use high-fidelity large eddy simulation (LES) data of separated compression ramp STBLI flows at supersonic to hypersonic conditions (Helm & Martin 2015, 2016; Trichilo, Helm & Martin 2019; Helm & Martín 2020) to analyse the properties of mixing layers in hypersonic separated flow with the intention of contributing to the research of mixing layer theory. Our flow conditions include free stream Mach numbers ranging from 3 to 10 which were found to produce shear layers with convective Mach number ranging from 1 to 2. This highlights an attractive feature of STBLI separation shear layers in that they

naturally occur at high convective Mach number. They also present the rare combination of high convective Mach number with reverse flow on the low-speed side. A further detail of the STBLI shear layers is that they exists in an adverse pressure gradient. We find that the pressure increases approximately linearly in the direction of shear layer development and that similarity in the mean velocity and turbulent stress profiles is still achieved under these conditions. Because we are using high-fidelity, high detail LES data, we are able to obtain accurate turbulence statistics in the shear layer. The spatial/temporal resolution of the LES data also allows us to produce statistics on the shear layer turbulence structures, to visualize instantaneous realizations of the turbulence structures, and to directly calculate their convection velocity. The vortex convection velocity is an important parameter in characterizing the mixing layer yet it is notoriously difficult to measure accurately in experiments (Barre *et al.* 1994; Dupont, Muscat & Dussauge 1999; Thurow *et al.* 2008).

In this paper we first provide in § 2 an overview of the STBLI data used for this study. In § 3, the mean flow properties of the shear layer are tabulated. The form of the shear layer vortices is the topic of § 4. The shear layer turbulence properties including turbulent kinetic energy (TKE) and Reynolds stress budgets are compared with available mixing layer data and theory in § 5 followed by a summary of conclusions in § 6.

2. LES database

For this study we use the data of Helm & Martín (2020) who, together with Helm & Martin (2016), Helm & Martin (2015) and Trichilo *et al.* (2019), perform a validation of the LES data against DNS of shock and turbulent boundary layer interactions. Detailed comparisons of mean and intensity profiles and spectral distributions show the accuracy and the high fidelity of the LES data, which include compression ramp-generated STBLIs at free stream Mach numbers of 3, 7 and 10. These are referred to throughout this paper as cases M3, M7 and M10, respectively. All three flows are two-dimensional (2-D) in the sense that they are of a flat plate boundary layer over a 2-D wedge and are assumed to be homogeneous in the spanwise direction. All three flows are strong interactions and are fully separated in the mean. The shear layer that forms over the separation bubble is the focus of the current research. The selection of the flow conditions was dictated by the experimental and DNS data available for validation of the LES, and the disparate conditions here give the conclusions broader applicability.

The LES coordinate axes are indicated by capital letters (X, Y, Z) and refer to the streamwise, spanwise and wall-normal directions, respectively. The shear layer coordinate axes, to be explained in § 3, are specified by the lowercase letters (x, y, z) where x is in the direction of the shear layer development, y is the spanwise direction and z the cross-stream direction. Unless stated otherwise, the velocity components (u, v, w) are in the direction of the mixing layer coordinate system. The computational grids are provided in table 1. Included in table 1 are the ramp angle φ, the simulation reference boundary layer thickness δ_o, the outer dimensions of the computational domain in units of δ_o, the grid resolution in units of the incoming boundary layer inner length scale and the number of grid points. The outer dimensions include the length of the wall from inlet to the corner L_{X1}, the length of the ramp surface from the corner to the outlet L_{X2}, the span width L_Y and the height of the grid at the inlet plane L_Z. The grid resolution is stretched in the streamwise direction so that Δx^+ is greatest at the inlet and smallest at the ramp corner. The spanwise resolution Δy^+ is uniform throughout. The first grid point away from the wall is given by z_2^+. The high bandwidth resolving efficiency of our numerical methods is comparable to linear Padé schemes in smooth regions (Martín *et al.* 2006; Taylor & Martín 2007; Taylor, Wu & Martín 2007; Wu & Martín 2007; Taylor & Martín 2008), and this, together with the

Case	φ	δ_o (mm)	L_{X1}/δ_o	L_{X2}/δ_o	L_Y/δ_o	L_Z/δ_o	Δx^+	Δy^+	z_2^+	Grid size
M3	24°	7.0	8	6.5	4	4.5	26.7–12.5	15.0	0.37	$280 \times 128 \times 65$
M7	33°	5.0	12	12	10	8	26.6–11.3	8.4	0.23	$300 \times 256 \times 80$
M10	34°	18.0	13	12	10	7	27.7–10.5	7.1	0.20	$780 \times 664 \times 100$

Table 1. Computational grid.

Case	M_e	U_e (m s^{-1})	ρ_e (kg m^{-3})	T_e (K)	Re (m^{-1})	T_w/T_a	δ_{bl} (mm)	Re_θ	Re_τ	L/δ_{bl}
M3	2.92	610.3	0.075	109	6.06×10^6	1.0	7.9	3220	360	3.03
M7	7.17	1146.4	0.076	64	1.91×10^7	0.5	4.9	3720	210	5.73
M10	9.05	1410.7	0.040	58	1.37×10^7	0.3	19.7	8280	520	3.26

Table 2. Conditions of STBLI mean flow.

adaptive shock sensor for locally dynamic shock capturing (Wu & Martín 2007), result in reduced grid sizes that are adequate for the solution of turbulence flows as has been demonstrated, see for example Wu & Martín (2007) or Priebe & Martín (2012, 2020). We use the LES models of Martín, Piomelli & Candler (2000) and Martín (2000), which employ an algebraic combination of locally dynamic, purely dissipative eddy viscosity and locally dynamic, conservative energy exchange counterparts like those designed by Bardina, Ferziger & Reynolds (1980) for incompressible flows. More details about the computational set-up and data validation can be found in Helm & Martín (2020), Helm & Martin (2015, 2016) and Trichilo *et al.* (2019).

Conditions of the free stream flow, the incoming boundary layer and the mean separation length are listed in table 2. The conditions ahead of the shock at the incoming boundary layer edge are indicated by the subscript 'e'. The Mach number M_e, streamwise velocity U_e, temperature T_e and density ρ_e are listed together with the unit Reynolds number $Re = \rho_e U_e/\mu_e$ where μ_e is the kinematic viscosity. Also included is the ratio of wall temperature T_w to the adiabatic recovery temperature $T_a = T_e(1 + 0.9((\gamma - 1)/2)M_e^2)$ where γ is the ratio of specific heats. Note that the M3 case is an adiabatic simulation and that the M7 case and the M10 case are both cold-wall simulations. The conditions of the incoming boundary layer ahead of the interaction region are indicated by the boundary layer thickness δ_{bl} and several Reynolds numbers. The Reynolds number based on momentum thickness θ is defined as $Re_\theta = \rho_e U_e \theta/\mu_e$. The friction Reynolds number Re_τ is defined as $\rho_w u_\tau \delta_{bl}/\mu_w$ where u_τ is the friction velocity and the subscript 'w' refers to the condition at the wall. Lastly, the mean separation length L is provided.

During the LES runtime, primitive flow variables were output at a high sampling rate of $f = 20U_e/\delta_{bl}$ from several stations positioned along X in the computational domain. At each station, that is at a given i-grid point, data was recorded from each j- and k-grid point. The grid indices i, j and k refer to the streamwise, spanwise and wall-normal grid directions, respectively. For each Mach number case, there are a total of seven of these stations evenly spaced in X between $(X - X_{sep})/L = 0.3$ and 0.9 in the region of the mean separation bubble. Here X_{sep} refers to the location of the separation point in the time- and spanwise-averaged ramp flow. These high-resolution time signals are used for the enhanced correlations described in § 4.1 and also the flow visualizations in § 4.3.

3. Region of similarity in the mean separated flow

3.1. *Similarity profiles*

The STBLI separation shear layers are visualized in figure 1 by the region of elevated turbulence in the contours of mean turbulent kinetic energy TKE $= \overline{u_i' u_i'}/2{U_e}^2$. In each case, the shear layer forms at the foot of the shock and makes an angle to the wall surface. The positions of the shock and the separation dividing streamline are also indicated in figure 1. A shear layer coordinate system (x, z) is defined for each case such that the longitudinal x-axis extends along the centre of the layer in the direction of its development and the z-axis is perpendicular to x in the cross-stream direction. Canonical mixing layers are characterized by a linear growth rate of the layer thickness (Tennekes & Lumley 1972; Lesieur 1987). If linear growth does in fact occur in the present shear flows, it should be possible to collapse profiles of the mean flow onto a single similarity profile by plotting against the similarity variable $\zeta = z/x$. In doing so, a region of approximate linear growth is found in each of the three STBLI flows.

The mean velocity and mean turbulence stresses are plotted versus ζ for M3, M7 and M10 in figures 2–4, respectively. Obtaining these profiles required the positioning of the shear layer coordinate system xz-axes, the rotation of which was determined by the orientation of the mean velocity field, and the origin by the angle of spread observed in the contour of mean TKE. This manual placement of the mixing layer coordinates is similar to the method used by Dupont *et al.* (2019). The position of the xz-axes for each case are shown in figure 1. The angles of inclination for the Mach 3, 7 and 10 flows are 12.0°, 8.5° and 10.0°, respectively. The bold dashed lines in figure 1 indicate the range in x for which a good collapse of the similarity profiles was found. The profiles of figures 2–4 were taken from this range.

The collapsed profiles themselves resemble quite well those of the classic mixing layer. The mean longitudinal velocity profiles show high and low velocities connected by a single inflection point, and the profiles of turbulence stress are approximately Gaussian with the peak coinciding with the location of the inflection point in the mean velocity U. Both of these features are typical of the canonical mixing layer and together they produce the Kelvin–Helmholtz inviscid instability (White 1974). Unlike the classic mixing layer similarity solution, the collapsed profiles for all three shear layers appear to be non-symmetric with the turbulence peak (equivalently the inflection point in the mean velocity) biased towards the high-speed side of the layer. It is shown in § 5 that this bias is a result of the proximity of the wall on the low-speed side. The profiles of mean cross-stream velocity show that W is essentially zero across the layer for all three cases indicating that the mean velocity is nearly parallel to the x-axis. The minimal variation in W across the layer is also consistent with a reduced entrainment rate, and therefore reduced spreading rate as is expected for highly compressible mixing layers. This point is discussed further in § 3.4.

3.2. *Two stream flow properties*

Encouraged by the quality of collapse of the profiles as well as their resemblance to the canonical free mixing layer flow, we make an attempt to categorize these STBLI shear layers in the manner of conventional compressible mixing layers. To do so we must describe each shear layer as two streams, a high- and a low-speed stream, each with constant velocity and constant thermodynamic properties. As can be seen in figures 3–5 this will only be an approximation as all profiles deviate from the typical mixing layer solution near the edges of the layer. Spreading occurs at the low-speed end of the profiles

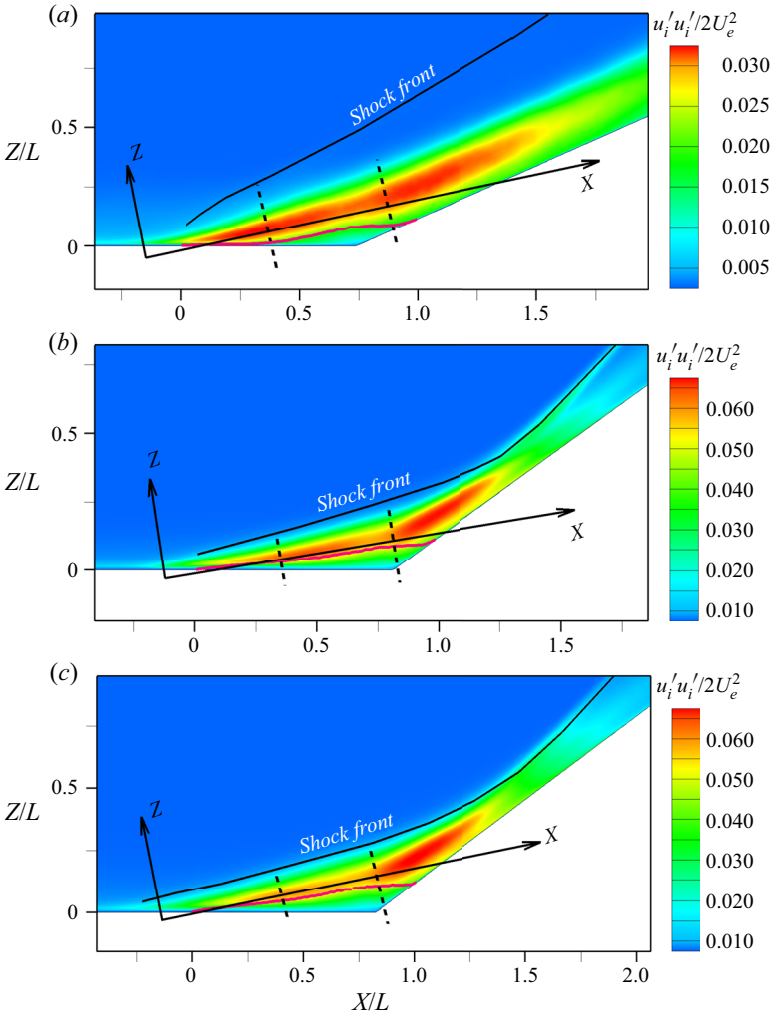

Figure 1. Mixing layer coordinate system definition for the (*a*) Mach 3, (*b*) Mach 7 and (*c*) Mach 10 compression ramp datasets. Contours are of the turbulent kinetic energy, TKE $= u_i'u_i'/2U_e{}^2$. The black line is the location of the mean shock front and the magenta line is the mean dividing streamline. Dashed lines indicate the range of similarity.

due to the presence of the wall and at the high-speed end due to the presence of the separation shock (the location of the shock in ζ is easily seen in the profiles of W). It will be shown, however, that even a rough estimation of the mean properties of the two streams is sufficient for a general comparison to canonical mixing layer data. The estimations of the two stream properties for each shear layer are listed in table 2. The methods for determining the entries of table 2 are discussed below. By convention, properties associated with the high-speed side are indicated with the subscript '1' and the low-speed side with subscript '2'.

The velocity U_1 and temperature T_1 for each case are estimated as the inviscid post-shock solution for the STBLI free stream undergoing a flow deflection equal to the angle of inclination of the x-axis. This selection of U_1 and T_1 stems from the observation that the rotated mean W profiles are essentially zero for all three shear layers. It is worth

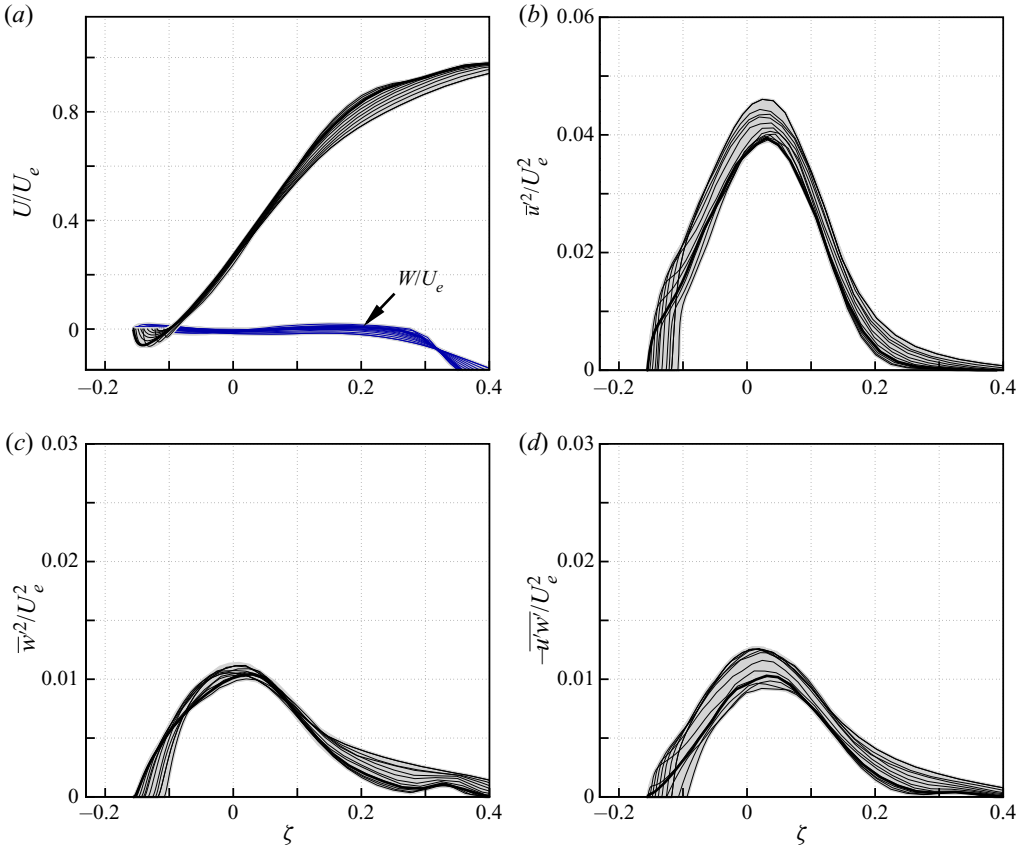

Figure 2. Similarity profiles in the Mach 3 STBLI separated shear layer: (*a*) the mean axial and cross-stream velocity; (*b*) axial turbulence intensity; (*c*) cross-stream turbulence intensity; and (*d*) turbulence shear stress. The bold line is the profile at the ramp corner.

noting that we found the initial deflection angle of the separation shock, as shown for each case in figure 1, corresponds closely to the resulting wave angle of the oblique shock solution. The high-speed stream Mach number M_1 is determined from U_1 and T_1. The M7 and M10 flows maintain Mach number above 5 downstream of the separation shock and can be considered hypersonic shear layers.

The velocity U_2 of the low-speed side is estimated as the minimum in the similarity profiles of U in figures 2–4(*a*). The low-speed side T_2 is likewise determined from the similarity profiles of temperature which are plotted in figure 5. All three cases show a satisfactory collapse of temperature within the previously defined range of approximate similarity. In each shear layer, however, there occurs a 'hook-off' of the temperature profiles on the low-speed side. This is due to the constant-temperature boundary condition at the wall. The wall temperature of the Mach 3 case is nearly adiabatic and so the divergence of the profiles in figure 5(*a*) is minimal. Because the Mach 7 and Mach 10 are both cold-wall simulations, the temperature drops significantly inside the separation bubble as seen in figure 5(*b*,*c*). The low-speed T_2 is therefore estimated as the maximum value in temperature just before the profiles diverge to meet the wall boundary condition. The two hypersonic shear layers have large temperature ratios such that T_2 experiences an increase of over five times T_1 for the M7 case and nearly seven times for the M10 case.

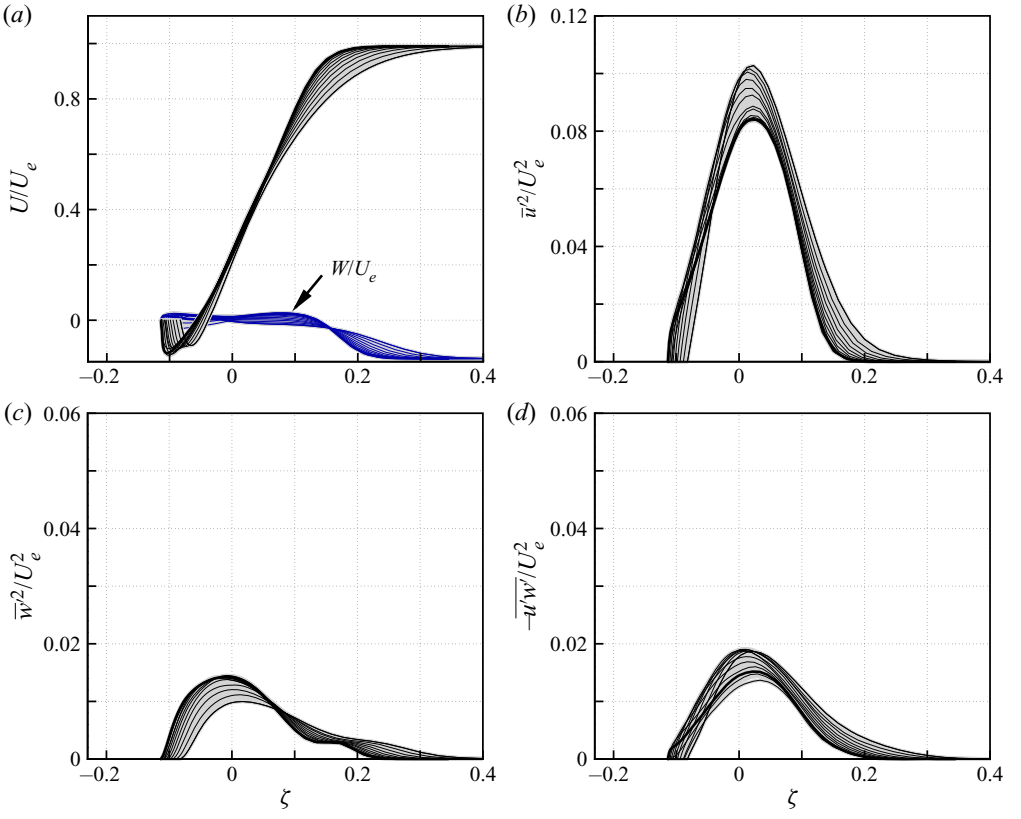

Figure 3. Similarity profiles in the Mach 7 STBLI separated shear layer: (*a*) the mean axial and cross-stream velocity; (*b*) axial turbulence intensity; (*c*) cross-stream turbulence intensity; and (*d*) turbulence shear stress. The bold line is the profile at the ramp corner.

In comparison, the M3 case T_2 is only double the value of T_1. Also listed in table 2 is the low-speed stream Mach number M_2 calculated from U_2 and T_2.

Because the separated flow is shock-induced, an adverse pressure gradient occurs along the length of the shear layer. Figure 6 shows that the pressure increases nearly linearly along the x-axis for all three cases. The reference pressure p_1 is the post-shock pressure from the oblique shock solution from which U_1 and T_1 are obtained. The average rate of pressure increase $\mathrm{d}p/\mathrm{d}x$ in units of p_1/L was determined from a linear fit to the data of figure 6. For the Mach 3 flow the pressure increases by nearly 50 % across the region of similarity, while for the Mach 7 and Mach 10 flows the pressure approximately doubles. As a result of the adverse pressure gradient, the mean density plotted versus ζ does not collapse when normalized by the free stream density as is apparent in figures 7(*a*), 7(*c*) and 7(*d*). The density is seen to increase significantly from the most upstream profile to the most downstream profile. However, a much better collapse is achieved if each individual profile of ρ is non-dimensionalized by the local $\rho_2(x)$. The inverse of ρ non-dimensionalized by $\rho_2(x)$ is plotted in figures 7(*b*), 7(*d*) and 7(*f*). That is, although there is a monotonic increase in density along x, the ratio between the two streams is approximately constant. Therefore, only the density ratio $s = \rho_2/\rho_1$ is reported in table 2. The value of local $\rho_2(x)$ was determined from the individual profiles in figure 7(*a–c*) in a manner similar to the selection of T_2 from the profiles of temperature. Note that the

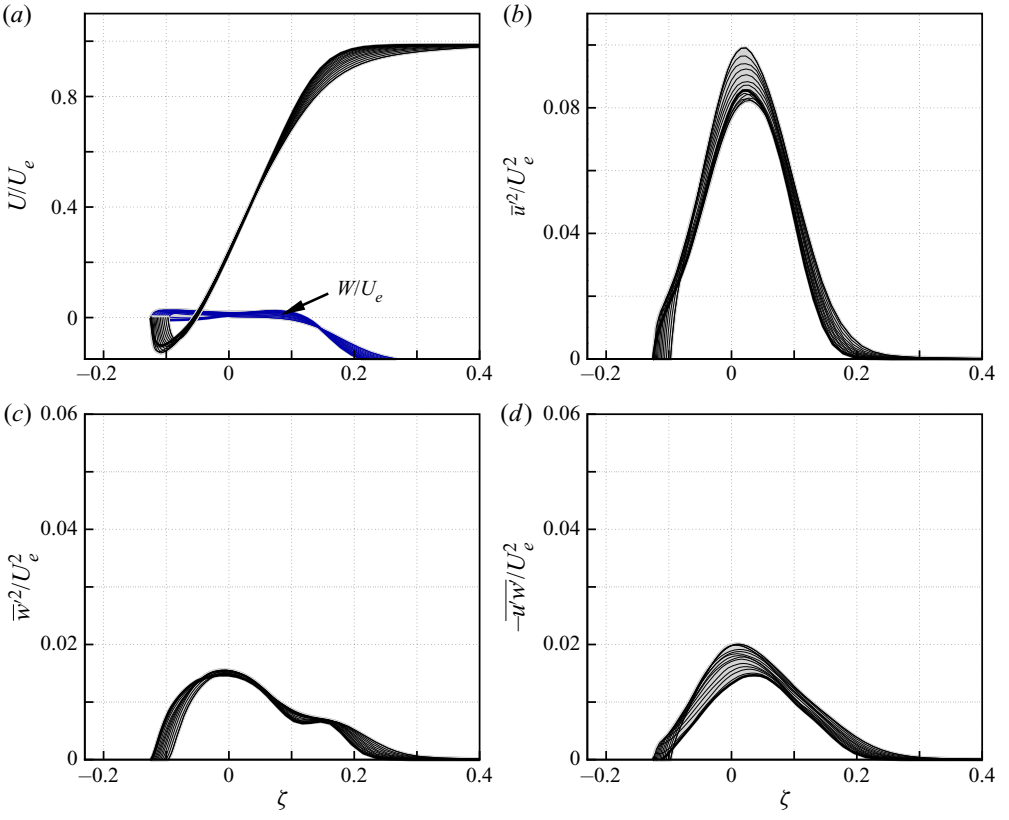

Figure 4. Similarity profiles in the Mach 10 STBLI separated shear layer: (*a*) the mean axial and cross-stream velocity; (*b*) axial turbulence intensity; (*c*) cross-stream turbulence intensity; and (*d*) turbulence shear stress. The bold line is the profile at the ramp corner.

density could have equivalently been non-dimensionalized by the local $\rho_1(x)$ to obtain the collapse. We chose to use $\rho_2(x)$ because this quantity was easier to select from figure 7(*a–c*). The Mach 3 STBLI flow produces a density ratio of approximately $1/2$ across the shear layer while both the Mach 7 and Mach 10 interactions produce a density ratio of $1/3$. Also included in table 2 is the velocity ratio $r = U_2/U_1$ for each case.

3.3. *Convective Mach number*

Now that the properties of the shear layer high- and low-speed streams are known, the theoretical convective Mach number defined as

$$M_c = \frac{U_1 - U_2}{a_1 + a_2} \tag{3.1}$$

and also the theoretical mixing layer vortex convection velocity $U_{c,i}$ defined as

$$U_{c,i} = \frac{a_1 U_2 + a_2 U_1}{a_1 + a_2} \tag{3.2}$$

can be calculated for these flows. These expressions for the convective Mach number and convective velocity are derived for an isentropic mixing layer where a_1 and a_2 are the speed of sound in the two streams (Bogdanoff 1983; Papamoscho & Roshko 1988). The M_c and

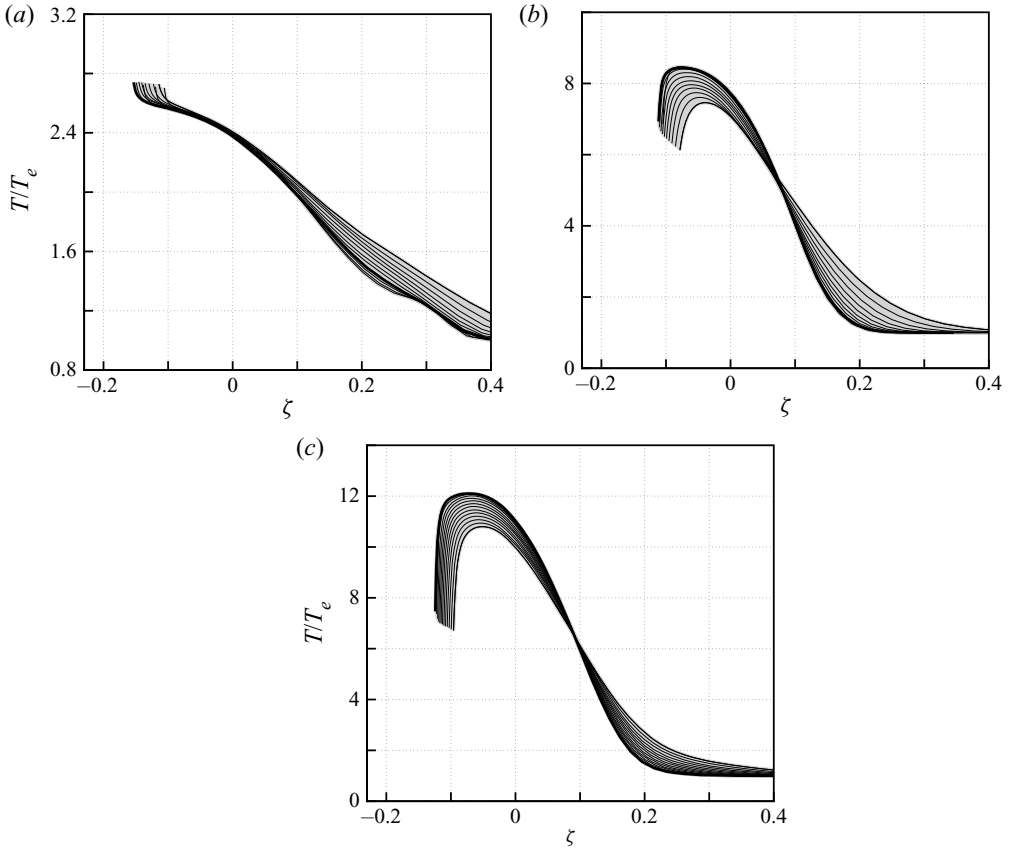

Figure 5. Similarity profiles of temperature in the (*a*) Mach 3, (*b*) Mach 7 and (*c*) Mach 10 STBLI separated shear layers.

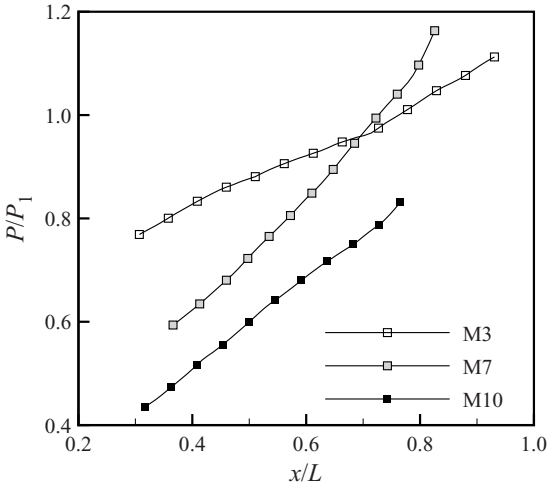

Figure 6. Pressure gradient along the shear layer centreline.

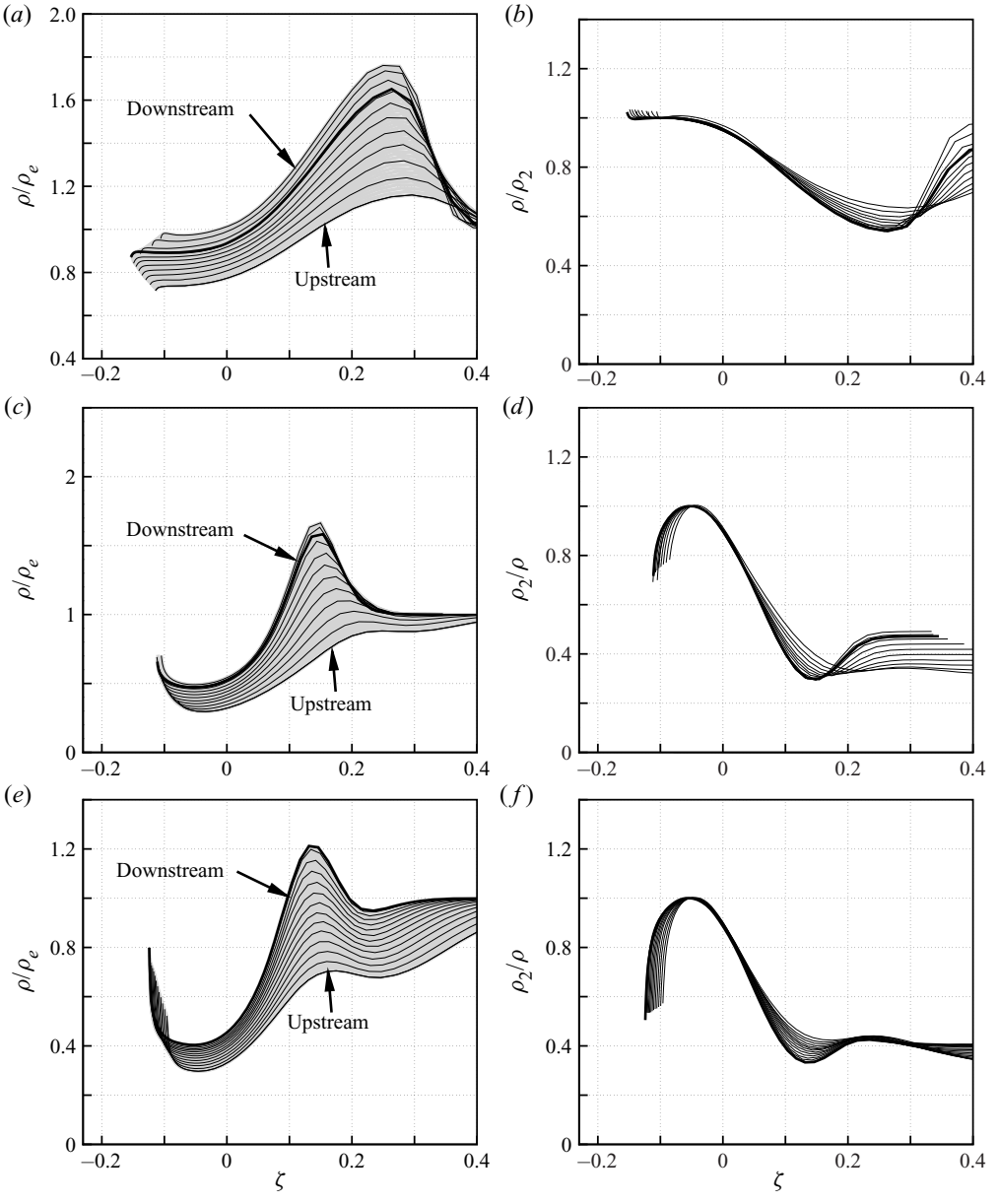

Figure 7. Similarity profiles of density in the (*a*,*b*) Mach 3, (*c*,*d*) Mach 7 and (*e*,*f*) Mach 10 STBLI separated shear layers. The profiles in panels (*a*,*c*,*e*) are normalized by the free stream density. Panels (*b*,*d*,*f*) are profiles of the inverse density normalized by the density of the low-speed side, that is, ρ_2/ρ. Plotting density in this way shows the variation in $s = \rho_2/\rho_1$.

$U_{c,i}$ are computed for each case and listed in table 3. An interesting feature of the separated STBLI flows is that they produce shear layers with rather high M_c even for the Mach 3 compression ramp flow. All three shear layers are above $M_c = 1$. This is an attractive feature considering that the majority of mixing layer data available today, particularly for turbulence statistics, is below $M_c = 1$.

Case	U_1 (m s^{-1})	T_1 (K)	M_1	U_2 (m s^{-1})	T_2 (K)	M_2	$\mathrm{d}p/\mathrm{d}x$ (p_1 L^{-1})	s	r	M_c	$U_{c,i}$ (m s^{-1})
M3	551	140	2.3	−36	279	0.1	0.52	0.541	−0.065	1.03	308
M7	1115	99	5.6	−137	537	0.3	1.20	0.299	−0.123	1.89	739
M10	1368	115	6.3	−142	707	0.2	0.86	0.333	−0.104	1.99	934

Table 3. Averaged mixing layer flow properties.

Case	$\delta'_{u'}$	$\delta'_{u'w'}$	δ'_{inc}	$\delta'_{u'}/\delta'_{inc}$	$\delta'_{u'w'}/\delta'_{inc}$
M3	0.265	0.238	0.311	0.853	0.766
M7	0.195	0.194	0.297	0.656	0.653
M10	0.205	0.202	0.296	0.692	0.682

Table 4. Spreading rate estimates and comparison with incompressible theory.

For mixing layers with M_c above 1 it is likely that shock waves exist in one or both sides of the mixing layer, thus negating the isentropic assumption in the derivation of (3.1) and (3.2). We will show later in § 4.2 that the theoretical $U_{c,i}$ in table 3 is quite different from the convection velocity determined from enhanced two-point correlations.

3.4. *Spreading rate*

Despite its known limitations as a scaling parameter, the convective Mach number defined by (3.1) is currently the most widely accepted metric in the literature for classifying the compressibility effects of mixing layers (Smits & Dussauge 2006). One such classification is the observed significant decrease in layer spreading rate with increasing M_c. Smits & Dussauge (2006) presented a compilation of compressible mixing layer spreading rate data, expressed as a fraction of the spreading rate of an equivalent incompressible mixing layer with the same values of r and s, and plotted these versus M_c (see figure 6.6 in the reference). Included in the data compilation are the classic Langley curve (Birch & Eggers 1972; Kline *et al.* 1980), the semiempirical curve by Dimotakis (1991) and the linear stability analysis prediction of spreading rate decrease with M_c by Day *et al.* (1998). The data show that the spreading rate can decrease by as much as 50 % to 80 % from the incompressible case for M_c above 0.5. For the current data, normalized spreading rate predictions from the classic Langley curve are approximately 0.55 for the Mach 3 flow and 0.40 for both the Mach 7 and Mach 10 cases as determined by the values of M_c in table 3.

For the STBLI shear layers, the spreading rate of vorticity thickness $\delta' = \mathrm{d}\delta_\omega/\mathrm{d}x$ where $\delta_\omega = \Delta U/\max(\mathrm{d}U/\mathrm{d}z)$ can be estimated using the two different methods outlined by Dupont *et al.* (2019). The first of these uses a comparison of the normalized $\overline{u'^2}$ similarity profile with the same from an incompressible mixing layer. Here the two-stream mixing layer data of Mehta & Westphal (1984) (figure 5*b* in the reference) is used. This first method assumes that the shape of the $\overline{u'^2}$ profile as well as the ratio of $(\mathrm{d}\delta_\omega/\mathrm{d}x)/\mathrm{d}\zeta$ do not differ between the compressible and the incompressible cases. The second method involves fitting a Gaussian curve to the profiles of turbulent shear stress. Both methods provide consistent results. These are listed in table 4.

A theoretical estimate of the spreading rate for an incompressible mixing layer with non-zero density ratio s can be determined from the relation derived by Papamoscho &

Roshko (1988),

$$\delta'_{inc} = \delta'_{ref} \frac{(1-r)(1+\sqrt{s})}{(1+r\sqrt{s})}. \tag{3.3}$$

In (3.3), δ'_{ref} is a reference spreading rate from an incompressible mixing layer with $s = 1$ and $U_2 = 0$ and is typically taken to be equal to 0.16 (Smits & Dussauge 2006). The STBLI shear layer spreading rates are also listed in table 4 as a fraction of the corresponding incompressible estimate. The spreading rate ratios are less than unity, however, they are approximately 50 % to 70 % higher than the Langley curve predictions. The Langley curve, however, is based primarily on data for single or two stream coflowing mixing layers. It has been shown that the spreading rate can be significantly greater for counter-current mixing layers (Strykowski *et al.* 1996; Forliti, Tang & Strykowski 2005) and also for mixing layers subjected to adverse pressure gradients (König, Schulülter & Fiedler 1998). Although there is significantly less data on the counter-current mixing layer than the coflowing configuration, one notable work is that of Strykowski *et al.* (1996). The authors performed a series of counter-flowing axisymmetric jet experiments at $M_c \approx 1$ with varying reverse flow strength. They showed that the spreading rates were consistently 60 % greater than the case of a single stream jet. Another consideration is that (3.3) might not be an accurate approximation for the spreading rate of incompressible counter-current mixing layers. Strykowski *et al.* (1996), however, also showed that (3.3) was valid for their experimental data if the reverse flow strength did not exceed $r < -0.1$. Even so, the disagreement for $r < -0.1$ was cited by the authors as possibly due to an artefact of their jet nozzle. At any rate, the shear layer data in table 4 clearly shows a decrease in spreading rate from the M3 case at $M_c \approx 1$ to the M7 and M10 cases at $M_c \approx 2$.

4. Vortex signature and convection velocity

The similarity profiles of the mean velocity and turbulence stresses presented in § 3.1 indicate that the criteria for the inviscid Kelvin–Helmholtz instability exist in the STBLI shear layers, and so it is expected that there will be large spanwise-oriented vortices present in the flow. Changes in the global characteristics of the compressible mixing layer as compared with the incompressible condition may be better understood through observation of the dynamics of the large vortical structures. The detection and description of the average signature of these vortices is the subject of this section.

4.1. *Enhanced correlation method*

A schematic of the shear layer in the compression ramp STBLI flow is given in figure 8. In panel (*a*) is shown a model of the spatial development of the mixing layer structures as they convect along the x-axis. It is assumed that the vortices convect at a constant velocity U_c and that they follow one after the other at fairly regular intervals. It is also assumed that they do not stray too far from the shear layer centreline. At reattachment the vortices are shed into the downstream flow. These assumptions are based on observations of the temporally resolved and spatially resolved LES data and are verified in § 4.3 by the instantaneous vortex visualizations. If the flow is probed at a stationary point in the shear layer, the resulting time signals can be converted to spatially 'frozen' turbulence via Taylor's hypothesis. This is drawn schematically in figure 8(*b*). The average signature of the frozen turbulence can be determined from the cross-correlations of the time signals of mass flux and pressure fluctuations in the following way. Consider for example the time signal of pressure taken from a point along the centreline of the shear layer. As a vortex

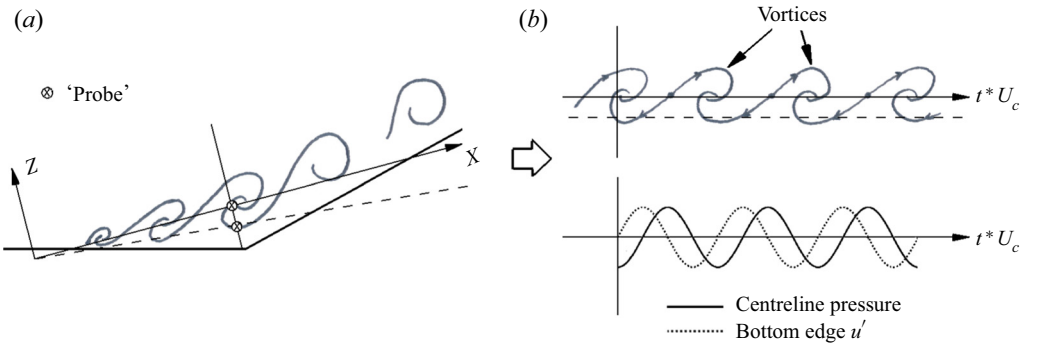

Figure 8. Schematic of the vortex structures (*a*) in the spatially developing shear layer in the separated compression ramp STBLI flow and (*b*) time signals taken from within the shear layer converted to 'frozen' vortices by using Taylor's hypothesis.

core convects past the probe location there will be a negative fluctuation in the pressure. Likewise, in-between successive vortices there will be a positive pressure fluctuation from the stagnation point in the convective reference frame. In a similar way, the time signal of longitudinal mass fluctuations $(\rho u)'$ taken near the bottom edge of the shear layer will give information on the aperiodic signature of the passing vortices due to the orientation of the vortex rotation. Taking the cross-correlation between the centreline p' and the bottom edge $(\rho u)'$ time signals produces a sinusoidal signature, the period of which is equal to the average time between successive vortices as they convect past the probe points. Although not shown in the schematic of figure 8, similar arguments can be made for cross-correlations between centreline p' and centreline cross-stream momentum $(\rho w)'$. Here we consider both $R_{(\rho u)'p'}$ and $R_{(\rho w)'p'}$.

A similar cross-correlation method was demonstrated by Kiya & Sasaki (1983) and also Cherry, Hillier & Latour (1984) for an incompressible separation shear layer, and Samimy *et al.* (1992) for compressible mixing layers. There are a couple of points to be made regarding the cross-correlation method used here. First, the signal of longitudinal momentum fluctuations could be taken from either the top or bottom edge of the shear layer. Kiya & Sasaki (1983), for example, used the high-speed edge. In this analysis, the bottom edge was chosen so as to avoid the separation shock. Second, autocorrelations of pressure with itself will also give a periodic correlation curve as demonstrated by Kiya & Sasaki (1983), Cherry *et al.* (1984) and Samimy *et al.* (1992). Here cross-correlations of p' and $(\rho u)'$, and also p' and $(\rho w)'$, were used in order to couple the mass flux and pressure field events, that is, to ensure that a pressure fluctuation is accompanied by a corresponding mass fluctuation. We found this strategy also ensures a more robust selection method for the enhanced correlation technique to be described shortly. Last, it was found that nearly identical correlation signatures were achieved when correlating velocity with pressure compared with correlating mass flux with pressure. In general the mass flux correlations provided a stronger signature and so only the mass flux and pressure correlations are included in this paper.

The details of the correlation method are as follows. Before calculating the cross-correlations, the signals of pressure and velocity are first bandpass-filtered in time. Fully separated STBLI flows are characterized by frequency spectra consisting of three distinct broadband ranges of energized turbulence motions. These are associated with (i) the inherent low-frequency unsteadiness of the separated flow; (ii) the mixing layer vortices; and (iii) the fine scale boundary layer turbulence. To demonstrate these frequency

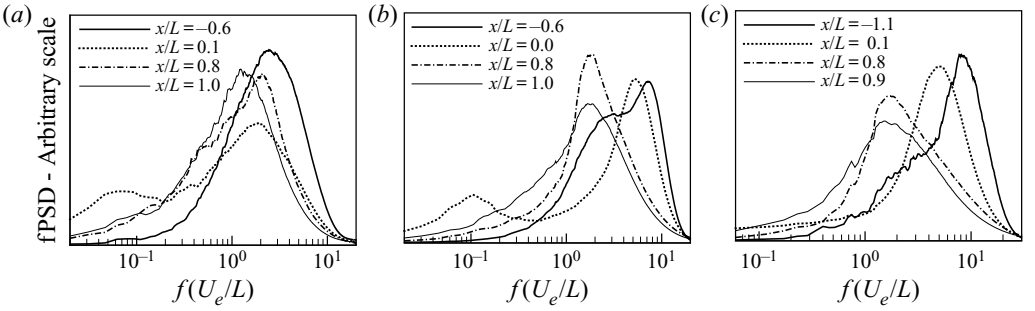

Figure 9. Premultiplied PSD of wall pressure signals from the (*a*) Mach 3, (*b*) Mach 7 and (*c*) the Mach 10 data. Spectra are shown for the upstream boundary layer (solid bold), separation point (dotted), corner (dashed bold) and reattachment (solid).

bands, premultiplied power spectral density (PSD) of wall pressure taken in the upstream boundary layer, the mean separation point, the ramp corner and the mean reattachment point are plotted in figure 9 for each of the three STBLI flows. These spectra were calculated using Welch's method with eight time segments with 50 % overlap and then bin sampled with a bin width of 0.1 in the log scale. From these spectra it is possible to make out the shifts in the distribution of turbulence energy as the flow progresses through the separated region. In the boundary layer, only the high-frequency turbulence exists with little to no energy present at the lowest frequencies. The undisturbed boundary layer turbulence is generally centred at $St_\delta = f\delta_{bl}/U_e = 1$ and experiences a shift to $St_L = 1$ downstream of the shock. This shift in the boundary layer turbulence can be seen when comparing the broadband energy peaks between the most upstream and most downstream spectra. The low-frequency oscillations of the shock appear in the separation spectra. It is well documented in the literature that the low-frequency oscillations in quasi-2-D separated STBLI flows occur at $St_L = fL/U_e$ of the order of 0.01 (among many references, see for example Dupont, Haddad & Debiève (2006) for reflected shock interactions and Priebe & Martín (2012) for compression ramp interactions). The relative strength of the low-frequency oscillations diminishes downstream, however, there still remains elevated energy at these frequencies in the corner and reattachment spectra. Although not appearing as a distinct peak in the premultiplied PSD, a substantial increase in energy at frequencies of approximately $St_L = 0.5$ occurs in the corner and reattachment spectra when compared with the first two spectra profiles. The increase in energy content at these intermediate frequencies is attributed to the development of the mixing layer turbulence (Dupont *et al.* 2006). Because the three energized frequency ranges are separate from each other, even more so as the ratio L/δ_{bl} increases, it is possible to filter out both the low-frequency oscillations and the fine-scale boundary layer turbulence from the mixing layer time signals. Therefore, a bandpass filter is designed for each case to retain frequencies between $St_L = 0.3$ and $St_\delta = 0.2$. Note that the low-frequency cutoff scales on L and the high-frequency cutoff on δ_{bl}. Correlation curves of $R_{(\rho u)'p'}$ and $R_{(\rho w)'p'}$ from bandpass-filtered time signals taken from the corner profile in each of the Mach 3, 7 and 10 flows are plotted in figure 10(*a–c*). The corner profile refers to the slice through the mixing layer that intersects the ramp corner as drawn in figure 8(*a*). The signals of p' and $(\rho w)'$ are taken at $\zeta = 0$ on the x-axis and $(\rho u)'$ along the bottom edge of the shear layer at $\zeta = -0.06$. The time axis is oriented so that a positive time shift indicates a motion of the fluid, $(\rho u)'$ or $(\rho w)'$, that occurs before the correlated fluctuation in pressure. Time is non-dimensionalized by the preshock free stream velocity U_e and separation length L.

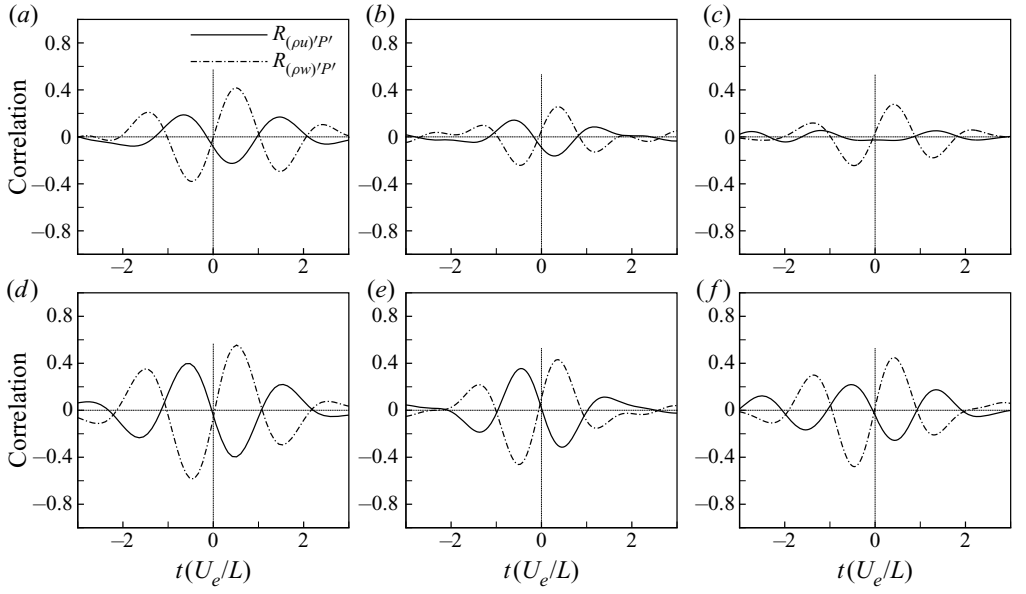

Figure 10. Cross-correlations between bandpass-filtered mixing layer centreline pressure and mass flux signals at the corner profile of each dataset. Averaged over full time signal (*a–c*) and enhanced average (*d–f*). (*a*,*d*) M3, (*b*,*e*) M7 and (*c*,*f*) M10.

Both the $R_{(\rho u)'p'}$ and $R_{(\rho w)'p'}$ curves are sinusoidal and are almost perfectly out of phase with each other. Only $R_{(\rho u)'p'}$ for the Mach 10 case fails to have a noticeable signature. A decrease in the mixing layer structure correlation level with increasing M_c was also observed by Samimy *et al.* (1992). The Mach 7 and Mach 10 flows, both $M_c \approx 2.0$, have a noticeably smaller amplitude than the Mach 3 with $M_c \approx 1.0$. The approximate period of the correlations is $2L/U_e$ which is consistent with the expected $St_L = 0.5$ for the mixing layer frequencies.

Although a distinct sinusoidal signature is visible in the full time signal correlations, the overall magnitude of the correlation is rather low particularly for M7 and M10. In order to obtain a stronger signature of the vortex events, an enhanced correlation method is used. The conditional averaging technique used here is similar to the method of Brown & Thomas (1977) for the detection of hairpin packets in a turbulent boundary layer. The strategy of Brown & Thomas assumes that the hairpin packet, or in this case the mixing layer vortex, is a specific isolated event occurring in the flow and that the corresponding fluid motion, or pressure fluctuation, associated with that event produces a specific signature in the time signal. Time signals of relevant fluid properties can be broken up into shorter segments and the cross-correlation computed for each of the shortened segments. If a vortex occurs in a given segment, the cross-correlation curve of that segment will produce the 'signature' of the vortex event. The enhanced correlation, therefore, is the average over all of the short-signal correlations that show the vortex signature.

For the detection of the mixing layer vortices, the time signals of p', $(\rho u)'$ and $(\rho w)'$ are broken up into N segments of length $6.5U_e/L$, or twice the wavelength of the bandpass filter low-frequency cutoff. Successive time segments are taken with 50 % overlap. We assume that the signature of the mixing layer vortices has the same form as the full time signal correlations. The criteria for the selection of the enhanced correlations are such that the segment correlations $R^n{}_{(\rho u)'p'}$ and $R^n{}_{(\rho w)'p'}$ simultaneously have maxima and minima

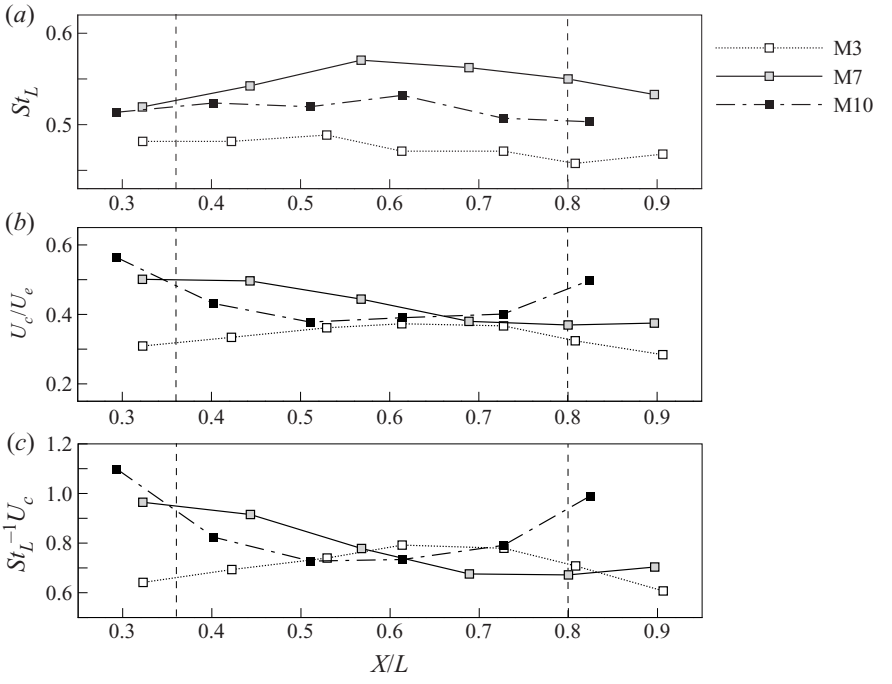

Figure 11. Non-dimensional vortex frequency (*a*), convection velocity (*b*) and length scale (*c*) determined from the enhanced correlations.

in the same location as, but at least twice the magnitude of, the full time average signature. More specifically, a correlation is retained if (i) $\max(R^n{}_{(\rho u)'p'}) \geqslant 2\max(R_{(\rho u)'p'})$ and (ii) $\min(R^n{}_{(\rho w)'p'}) \leqslant 2\min(R_{(\rho w)'p'})$ both in the range $-2 \leqslant \Delta t(U_e/L) \leqslant 0$ for $n \in N$. The enhanced results for the corner profile are shown in figure 10(*d–f*). For the Mach 3, approximately 30 % of the time segments met the criteria, and approximately 20 % for the Mach 7 and Mach 10 flows. A distinct wavelength appears in the enhanced correlation for all three cases including the Mach 10 $R_{(\rho u)'p'}$.

4.2. *Vortex convection velocity*

The enhanced correlation technique was repeated for several stations along the x-axis. The frequency in St_L determined from the $R_{(\rho u)'p'}$ enhanced correlation curve time period are plotted in figure 11(*a*) versus X/L. Although not shown, the time period selected from the enhanced correlations of $R_{(\rho w)'p'}$ produces similar frequencies to those from $R_{(\rho u)'p'}$. The frequency is approximately constant through the region of similarity for each case. Dupont *et al.* (2006) also showed that the shear layer frequency plateaus at a constant $St_L = 0.5$ in the separated flow of their reflected shock STBLI with free stream Mach number of 2.3. They also showed that this frequency was independent of the incident shock angle.

The enhanced correlations can be used to determine the actual mixing layer vortex convection velocity U_c. At a given position on the x-axis, if a time segment is selected by the enhanced correlation criteria, the centreline pressure signal from that time segment can be correlated with the same from an adjacent position along x. The convection velocity of that vortex event is then obtained by dividing the distance between the two points in x by the offset in time of the peak in $R_{p'p'}$. The U_c can then be averaged over all enhanced correlation selections. Here the cross-correlation of adjacent pressure signals is

used because the theoretical $U_{c,i}$ discussed in § 3.3 is by definition the convection velocity of the stagnation point between successive vortices (Papamoscho & Roshko 1988; Smits & Dussauge 2006). The averaged convection velocity versus X/L is plotted in figure 11(*b*). For the cross-correlations of pressure, adjacent points are spaced approximately $0.1L$ apart. An average of both the forward adjacent point and the backward adjacent point correlation is used to calculate U_c at each data point plotted in figure 11(*b*). The convection velocity seems to undergo a gradual transition in the first half of the similarity region, but, for all three flows, U_c levels off at $0.4U_e$ in the second half of the region of similarity. For comparison, $U_{c,i}$ calculated from (3.2) is $0.5U_e$ for the M3 flow and $0.6U_e$ for M7 and M10. A similar comparison was made by Dupont *et al.* (2006) for their Mach 2.3 reflected shock experiments. They found the phase velocity of wall pressure signals in the frequency range of $0.2 \leqslant St_L \leqslant 0.5$ gave a shear layer convection velocity of approximately $0.3U_e$ compared with the isentropic prediction of $0.5U_e$. In either case of the compression ramp or the reflected shock flow, the theoretical convection velocity significantly overpredicts the measured vortex convection velocity.

The time scale of figure 11(*a*) and the convection velocities of figure 11(*b*) can be combined to estimate the spatial wavelength of the frozen vortices. The spatial quantity $St_L^{-1}U_c$ is plotted in figure 11(*c*) and represents the average distance between successive vortex cores. As with the convection velocity, the wavelength seems to reach a constant value in the second half of the region of similarity, levelling off at approximately $0.8L$ spacing for all three flows.

4.3. *3-D vortex signature*

In order to investigate the spatial organization of the large vortex structure in our STBLI mixing layers, the following correlation coefficient is defined:

$$R_{f'p'} = \frac{\overline{f'(x+\Delta x, y+\Delta y, z+\Delta z)p'(x, y, z_{cl})}}{f'_{rms}p'_{rms}}, \tag{4.1}$$

where f' can refer to either $(\rho u)'$ or $(\rho w)'$, and $p'(x, y, z_{cl})$ is the pressure along the mixing layer centreline. Again Taylor's hypothesis of frozen vortices is used to convert time signals into spatial information and so, in (4.1), we set $x = tU_c$ where U_c is the convection velocity determined from the enhanced correlations described above. The enhanced spatial correlation can be generated in the same manner as the one-dimensional (1-D) correlations by averaging $R_{f'p'}$ over all time segments selected by the previously defined criteria. The enhanced spatial correlations of bandpass-filtered time signals from the corner profiles of the Mach 3, 7 and 10 flows are plotted in figures 12, 13 and 14, respectively. These plots represent the averaged 'frozen' spatial waveform of the mixing layer vortices as they convect past the corner profile as drawn schematically in figure 8. In figures 12–14, panel (*a*) is the enhanced average in the *xz*-plane for $\Delta y = 0$, and panel (*b*) is the enhanced average in the *xy*-plane for $R_{(\rho u)'p'}$. Panels (*c*) and (*d*) are the same for $R_{(\rho w)'p'}$. The *z*-location of the *xy*-plane is indicated by the solid black line in the corresponding panel (*a*) and also in panel (*c*). For $R_{(\rho u)'p'}$ the *xy*-plane is along the mixing layer bottom edge as was defined for the 1-D enhanced correlations. For $R_{(\rho w)'p'}$ the *xy*-plane is along the mixing layer centreline. Note that plotting the values of $R_{f'p'}$ along the line drawn in the *xz*-plane would result in the same 1-D correlation curves as in figure 10(*d–f*).

The form of the mixing layer vortices as determined from the 2-D correlation plots is a streamwise periodic structure that exists all through the cross-stream width of the

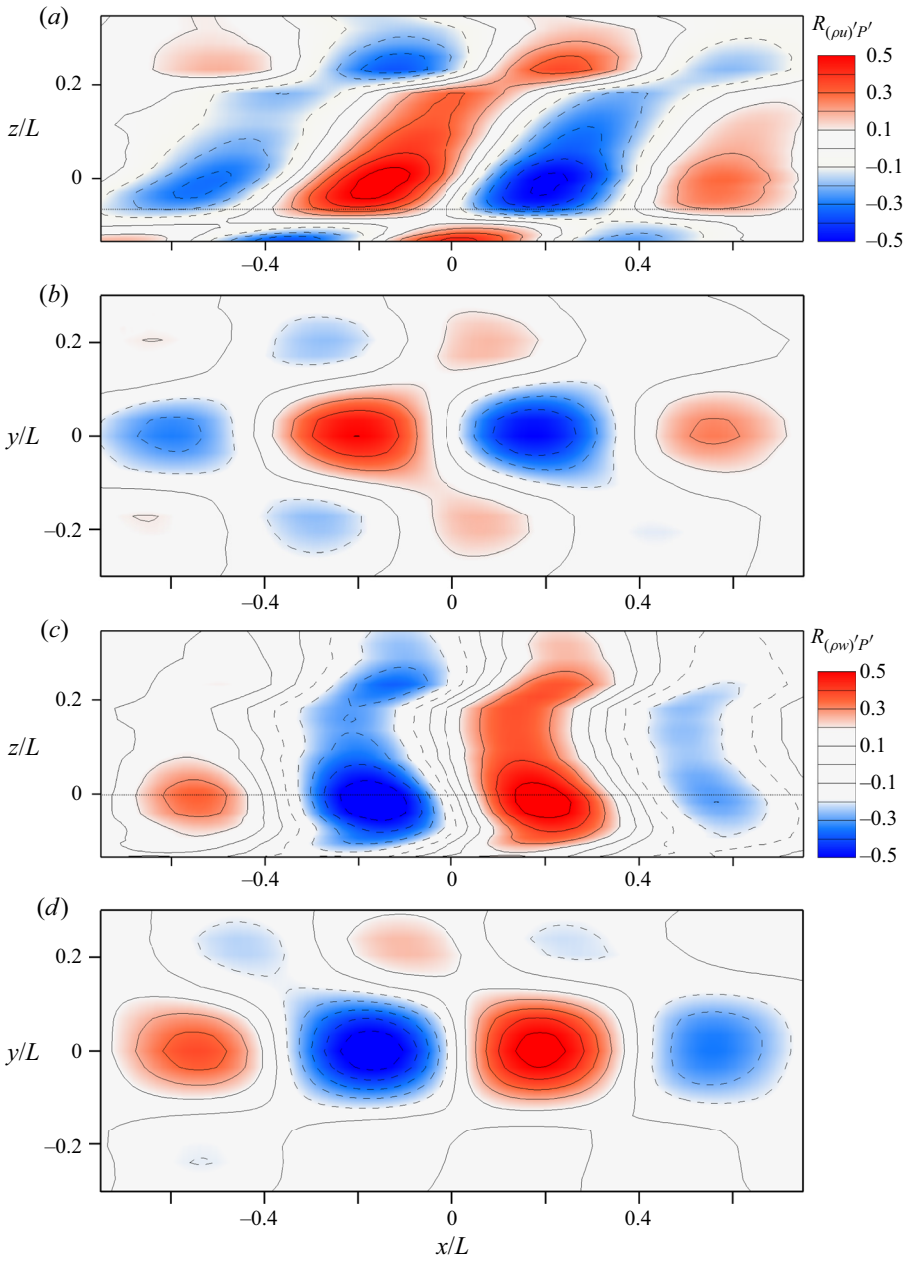

Figure 12. Enhanced correlation contours of the Mach 3 convective mixing layer structure. Correlations are of centreline pressure with longitudinal mass flux in (*a*) *xz*- and (*b*) *xy*-planes and centreline pressure with cross-stream mass flux in (*c*) *xz*- and (*d*) *xy*-planes. The horizontal dotted line in the *xz*-planes indicates the location of the corresponding *xy*-plane. Time correlations are converted to spatial information using the mixing layer convection velocity (i.e. $x/L = tU_c/L$).

mixing layer. In $R_{(\rho u)'p'}$, the sign of the periodic correlation is reversed in bands both above and below the mixing layer edges. These bands coincide with the position of the separation shock and the reverse flow, respectively. In the *xz*-plane, the coherent structures are tilted 'forward' in the correlations of streamwise mass flux and tilted 'backwards' in the

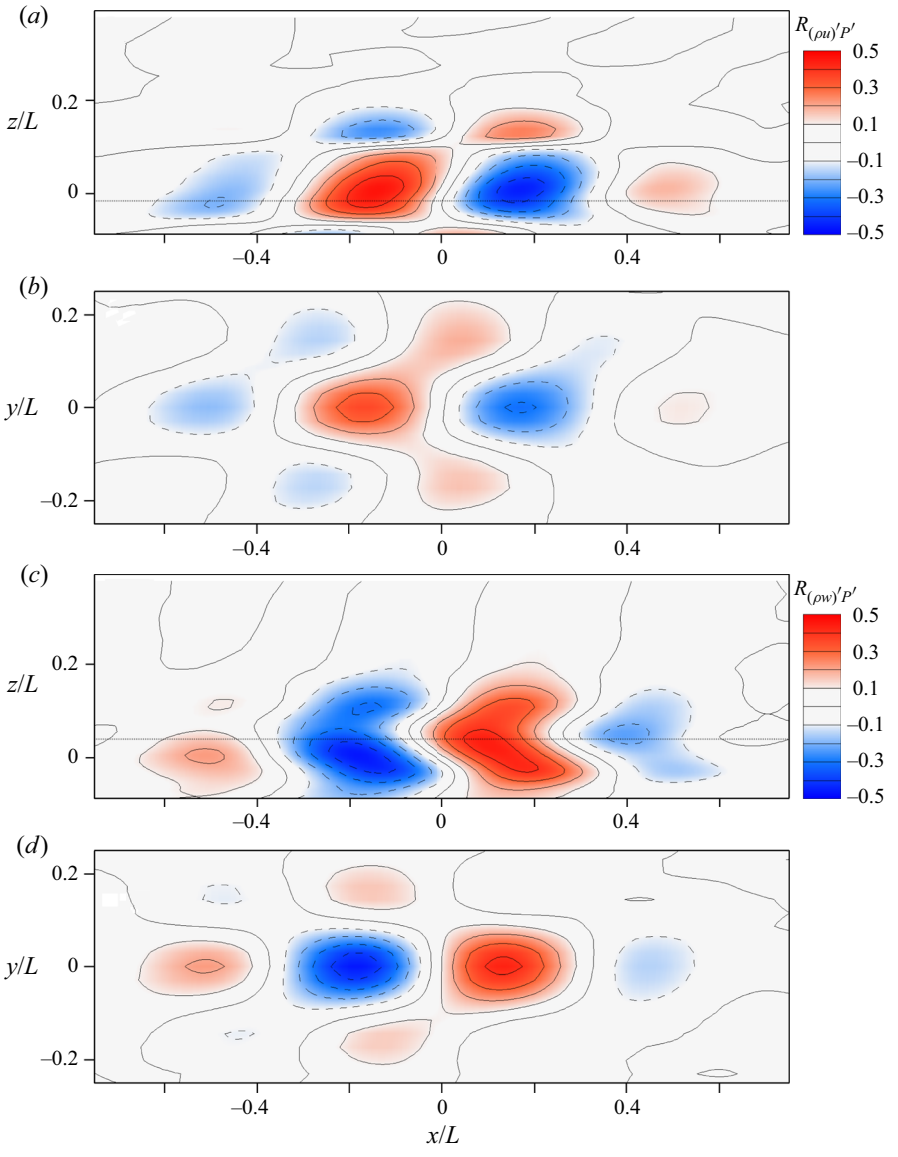

Figure 13. Enhanced correlation contours of the Mach 7 convective mixing layer structure. Correlations are of centreline pressure with longitudinal mass flux in (*a*) *xz*- and (*b*) *xy*-planes and centreline pressure with cross-stream mass flux in (*c*) *xz*- and (*d*) *xy*-planes. The horizontal dotted line in the *xz*-planes indicates the location of the corresponding *xy*-plane. Time correlations are converted to spatial information using the mixing layer convection velocity (i.e. $x/L = tU_c/L$).

correlation of the cross-stream mass flux. The horizontal axis in figures 12–14 is oriented so that positive Δx is 'downstream' and negative Δx is 'upstream'. In the *xy*-plane, an obvious oblique pattern occurs and the mixing layer structures do not appear as 2-D bands in the spanwise direction. This obliqueness in the average signature is consistent with compressible mixing layer research showing increased spanwise variation of the large mixing layer vortices with elevated convective Mach number (Sandham & Reynolds 1991; Clemens & Mungal 1992, 1995; Rossmann *et al.* 2002).

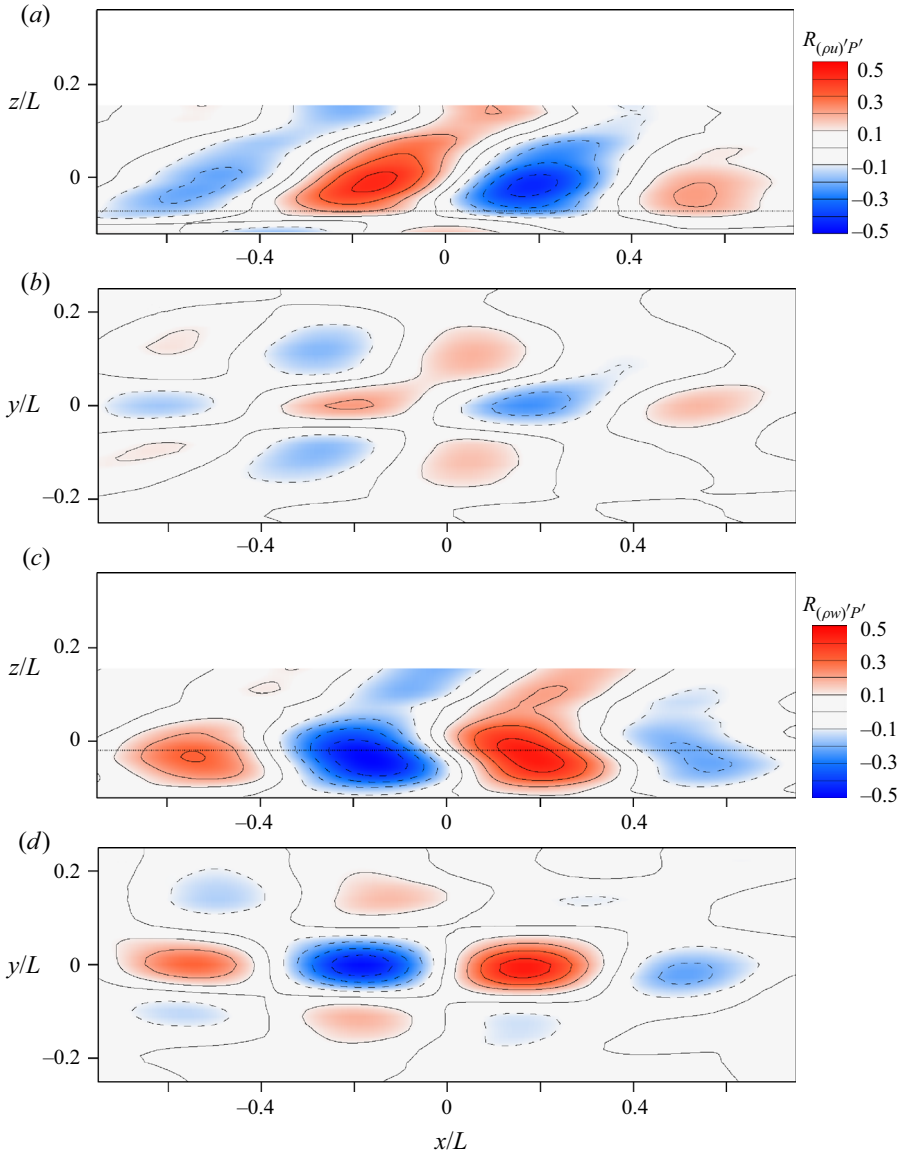

Figure 14. Enhanced correlation contours of the Mach 10 convective mixing layer structure. Correlations are of centreline pressure with longitudinal mass flux in (*a*) *xz*- and (*b*) *xy*-planes and centreline pressure with cross-stream mass flux in (*c*) *xz*- and (*d*) *xy*-planes. The horizontal dotted line in the *xz*-planes indicates the location of the corresponding *xy*-plane. Time correlations are converted to spatial information using the mixing layer convection velocity (i.e. $x/L = tU_c/L$).

The interpretation of the correlation contour plots can be aided by considering the vector field defined by the magnitude of $R_{(\rho u)'p'}$ and $R_{(\rho w)'p'}$. Assuming that a negative fluctuation in pressure coincides with a vortex core, a plot of the vector field defined by $-(R_{(\rho u)'p'}, R_{(\rho w)'p'})$ will provide information on the average motion about a mixing layer vortex centre. These are plotted in figure 15. Also plotted in figure 15 are the location of the mixing layer centreline and the inclination angles of the isolines of zero correlation from figures 12–14. The point of crossing of the zero-correlation isolines can be interpreted

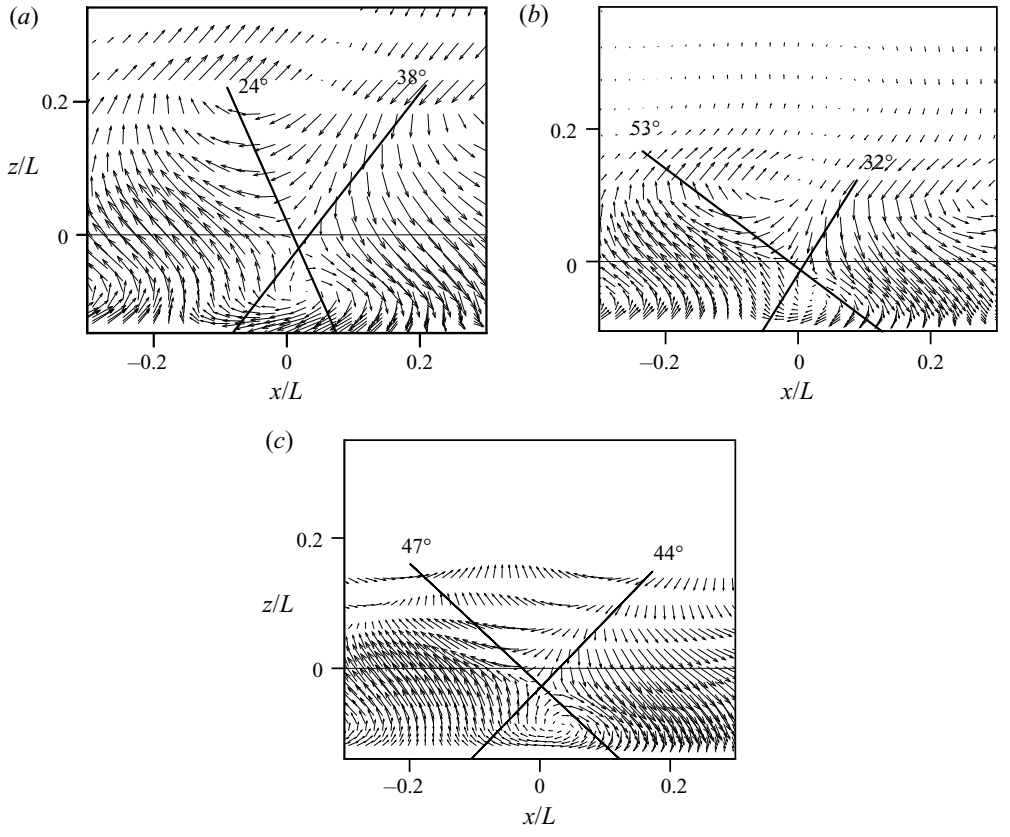

Figure 15. Vector fields of $-(R_{(\rho u)'p'}, R_{(\rho w)'p'})$ from figures 12–14 for (*a*) M3, (*b*) M7 and (*c*) M10. The vector field gives information on the averaged mass flux motion about a negative fluctuation in pressure. The horizontal line indicates the location of the mixing layer centreline. The inclination from vertical of the coherent structures as determined from the isoline of zero correlation in $R_{(\rho u)'p'}$ and $R_{(\rho w)'p'}$ are also indicated.

as the centre of the vortex. A similar correlation vector plot was used by Kiya & Sasaki (1983) for an incompressible separation shear layer. Unlike in Kiya & Sasaki, no clear rotational motion is observed around the vortex centre in figure 15. Instead, a saddle point occurs. The vector plot shows that the cross-stream momentum flux is positive to the left of the vortex core and negative to the right, as one would expect based on the (clockwise) orientation of the vortex roll-up. The vectors on the top and bottom of the vortex centre, however, are in the opposite orientation from what is expected. The interpretation of this stems from the fact that the density in the low-speed side of the layer is a factor of two less than on the high-speed side for the Mach 3 flow and a factor of four for the Mach 7 and 10 flows. The rotation of the vortex brings the low-momentum, low-density fluid into the high-speed, high-density side causing a negative streamwise correlation component to the left of the vortex centre. The opposite occurs for fluid being pulled from the high-speed side into the low-speed side to the right of the vortex centre.

Visualizations of the actual mixing layer vortices helps in asserting the interpretation of the enhanced correlation plots. Flow visualizations of individual mixing layer vortices in the raw data of the separated STBLI flows is made particularly difficult by the environment in which they reside. One must be able to separate specifically the mixing layer rollers from (i) the smaller scale vortical hairpin vortices in the incoming boundary layer turbulence

and (ii) the separation shock which sits very close to the high speed side of the mixing layer, as was shown in figure 1. We found that vortex detection methods based on the eigenvalues of the velocity divergence, such as swirl strength, were more problematic concerning the first issue. Vorticity methods, on the other hand, are dominated by the strong shear in the separation shock. Ultimately we found the method developed by Graftieaux, Michard & Grosjean (2001) to be the most robust for isolating the mixing layer vortices in the raw data. The Graftieaux method is based on the topology of the velocity field rather than on derivative quantities. It effectively searches the flow for points about which there is a net circulating motion and, because it uses a summation over a search window, it also acts as a spatial filter. This method was successively used by Dupont *et al.* (2008) to identify mixing layer vortices in particle image velocimetry (known as PIV) data from their separated reflected shock STBLI experiments.

The Graftieaux method is a vortex search method in a 2-D velocity vector field. If P is a point in the flow, S is a specified area surrounding P and M is a point inside S, the vector detector Γ_1 is defined by

$$\Gamma_1(P) = \frac{1}{S}\int_{M\in S} \frac{(\boldsymbol{PM}\times \boldsymbol{U_M})\cdot \boldsymbol{y}}{|\boldsymbol{PM}|\cdot|\boldsymbol{U_M}|}\mathrm{d}S = \frac{1}{S}\int_S \sin\theta_{\boldsymbol{M}}\,\mathrm{d}S, \tag{4.2}$$

where $\boldsymbol{PM}$ is the vector connecting points P and M. The velocity vector at point $\boldsymbol{M}$ is $\boldsymbol{U_M}$ and θ is the angle between the vectors $\boldsymbol{PM}$ and $\boldsymbol{U_M}$. The parameter Γ_1 will take on values between -1 and 1 where the sign depends on the direction of rotation. It can be shown that a vortex exists at $\boldsymbol{P}$ if $|\Gamma_1| > 2/\pi$. For a square interrogation area with N equally spaced discreet points inside the area S, (4.2) can be re-expressed as

$$\Gamma_1(P) = \frac{1}{S}\int_S \sin\theta_{\boldsymbol{M}}\,\mathrm{d}S = \frac{1}{N}\sum_N \sin\theta_{\boldsymbol{M}}. \tag{4.3}$$

The bandpass-filtered time signals of velocity from the corner profile of the ramp grids were again converted to space signals via the convection velocity of § 4.2. Thus the 3-D velocity field on which Γ_1 operates was generated. The 2-D velocity vector $\boldsymbol{U_M}$ is defined as $(u - U_c, w)$ and the Graftieaux vortex detector was applied throughout the volume but always in the xz-plane. A square interrogation window of size $0.5\delta_{bl}$ was used throughout. The results are plotted in figures 16–18. The contour of Γ_1 in the streamwise–spanwise plane sliced along the mixing layer centre ($\zeta = 0$) is plotted for a time segment equivalent to $8L$ in length that was randomly selected from the full time signal. This provides a top view of the instantaneous frozen mixing layer structures. In the inset of figures 16–18(b) is shown a side view of the structures. The location in the span of the 3-D volume of Γ_1 is indicated by the dashed line in the xy-plane contour. Similar plots are provided for arbitrarily selected time segments from the M3, M7 and M10 data.

From the top view, one can immediately observe the spanwise angular pattern in the vortices as is consistent with the 2-D correlation plots of figures 12–14. From the top plan view, the M3 vortices are visually more coherent than the M7 and M10 flows. Also, in the side view, the M3 vortices appear more regular and resemble a sinusoidal wavy interface between the high- and low-speed sides of the mixing layer. The vortex cores appear to occur predominantly at the upslope of the wave. A similar pattern is seen in the xz-plane slice of the M7 and M10 flows although, in general, the M3 flow is apparently more regular.

With regard to the spanwise oblique angle observed in both the enhanced correlation contours and the instantaneous vortex visualizations, it is interesting to consider the compressible mixing layer inviscid linear stability analysis by

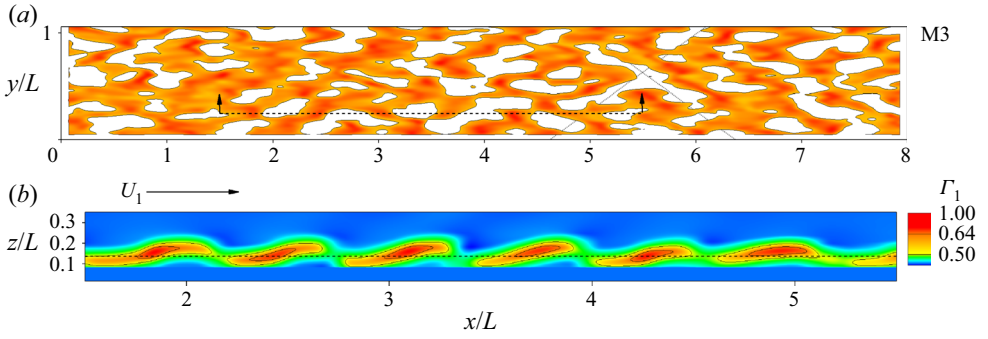

Figure 16. Contour of the vortex detector variable Γ_1 for the convective frozen flow from the corner grid plane of the Mach 3 flow. (*a*) The *xy*-plane sliced through the mixing layer centre and (*b*) the *xz*-plane sliced through the section indicated by the dashed lines and arrows in panel (*a*). Dotted diagonal lines indicate the vortex angle predicted by (4.4).

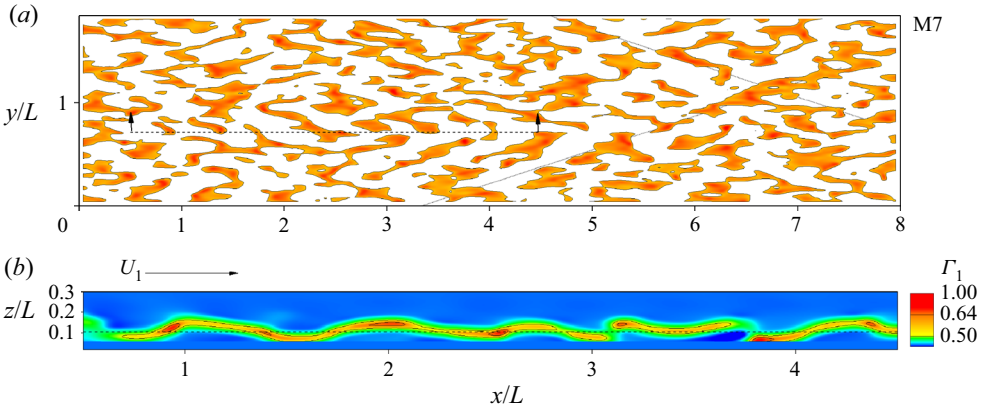

Figure 17. Contour of the vortex detector variable Γ_1 for the convective frozen flow from the corner grid plane of the Mach 7 flow. (*a*) The *xy*-plane sliced through the mixing layer centre and (*b*) the *xz*-plane sliced through the section indicated by the dashed lines and arrows in panel (*a*). Dotted diagonal lines indicate the vortex angle predicted by (4.4).

Sandham & Reynolds (1990, 1991). These authors showed that an oblique unstable mode becomes dominant over the 2-D mode for $M_c > 0.6$. Furthermore, they found that the angle α measured from the 2-D mode increased with increasing M_c by

$$M_c \cos\alpha \approx 0.6. \tag{4.4}$$

For the current STBLI shear layers, $\alpha = 54^\circ$ for the M3 flow and 72° for M7 and M10. These angles are indicated by the diagonal dotted lines drawn in the top-view contours of Γ_1 in figures 16–18(*a*) and prove to be a close representation of the actual structure occurring in these flows.

5. Turbulence scaling

Barre *et al.* (1994) used dimensional analysis of the free shear layer to show that the maximum turbulence shear stress $(-\overline{u'w'})_{max}$ non-dimensionalized by $U_c(U_1 - U_2)$ varies

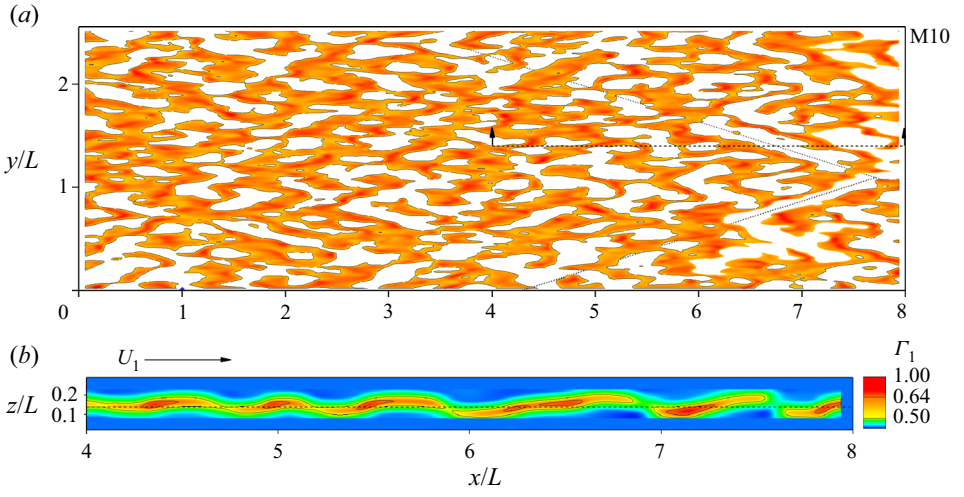

Figure 18. Contour of the vortex detector variable Γ_1 for the convective frozen flow from the corner grid plane of the Mach 10 flow. (*a*) The *xy*-plane sliced through the mixing layer centre and (*b*) the *xz*-plane sliced through the section indicated by the dashed lines and arrows in panel (*a*). Dotted diagonal lines indicate the vortex angle predicted by (4.4).

linearly with the vorticity spreading rate. Specifically

$$\delta' = \frac{1}{K}\frac{(-\overline{u'w'})_{max}}{U_c(U_1 - U_2)}, \tag{5.1}$$

where K is a proportionality constant to be determined empirically. The derivation of this relation is independent of M_c and therefore includes both compressible and incompressible layers. Oftentimes (5.1) is tested using $U_{c,i}$ for lack of a better estimate, but, as was shown in § 4, the actual convection velocity can vary significantly from the theoretical value. For the current flows, the error in $U_{c,i}$ is 25 % to 50 %. In figure 19 is plotted the maximum turbulent stress from the profiles in figures 2–4(*d*) versus the average of the two estimates of spreading rate from table 4. The maximum turbulence shear stress and maximum normal stresses are listed in table 5. Included in figure 19 are also the data of the separated STBLI shear layer from the experiments of Dupont *et al.* (2019), together with the subsonic counter-current mixing layer data of Forliti *et al.* (2005). It has been shown by Dupont *et al.* (2019) using a large compilation of incompressible and compressible shear layer data available from the literature that the majority of the coflowing and single-stream data fall within reasonable error of $K = 0.12$. The line drawn in figure 19 corresponds to this value of K. The dashed lines indicate the region of 10 % error. The incompressible, counter-current data of Forliti *et al.* show that the turbulence shear stress follows the $K = 0.12$ line for spreading rates below approximately 0.2. Above 0.2, a steeper linear trend occurs. This bifurcation in the Forliti data occurs between points of $r = -0.13$ and -0.19. Although the spreading rate is above 0.2, the Mach 3 data point with $r = -0.065$ follows the trend of the coflowing data. The Mach 7 and Mach 10 data points, which have stronger reverse flow ($r = -0.123$ and -0.104) than the Mach 3, lie within the trend of the Forliti data at the same spreading rate. The two data points of Dupont *et al.* have similar velocity ratios ($r = -0.057$ and -0.146) to the present STBLI shear layers and show the same trend of the stronger reversed flow case having a higher non-dimensionalized turbulent shear stress. The difference between the data of Dupont *et al.* and the current

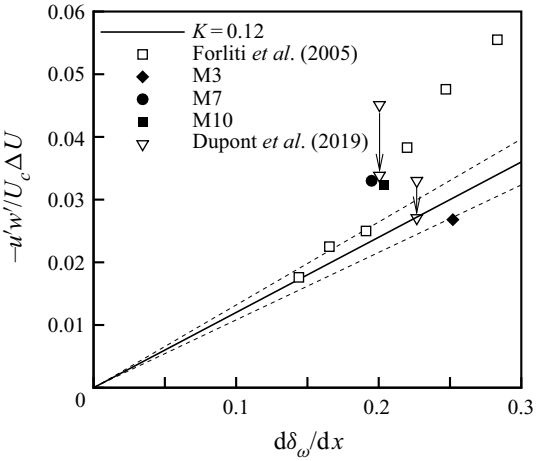

Figure 19. Non-dimensional turbulence stress versus the spreading rate. The arrows indicate how the data of Dupont *et al.* (2019) changes if ΔU is calculated in the same manner as the current data.

Case	$-\overline{u'w'}/U_c\Delta U$	$\overline{u'^2}/\Delta U$	$\overline{w'^2}/\Delta U$	$\overline{w'^2}/\overline{u'^2}$
M3	0.0268	0.0432	0.0108	0.250
M7	0.0330	0.0754	0.0117	0.155
M10	0.0323	0.0786	0.0131	0.167

Table 5. Reynolds stresses and anisotropy.

data may be related to the method of determining U_1 and U_2. Dupont *et al.* selected these values from a ζ closer to the mixing layer centre thus possibly underpredicting ΔU. If the method of § 3.2 is used to recalculate the ΔU of Dupont *et al.*, the two data points move much closer to the current data as indicated by the arrows in figure 19. This is an intriguing result and suggests that the change in the nature of the shear layer instability for counter-current mixing layers as described by Forliti *et al.* (2005) is independent of the level of compressibility.

The Reynolds stress anisotropy $\overline{w'^2}/\overline{u'^2}$ is known to be typically around 0.5 for incompressible shear layers and can decrease significantly for M_c above approximately 0.5 (Smits & Dussauge 2006; Dupont *et al.* 2019). Brown & Roshko (1974) used dimensional analysis to propose that the Reynolds stress anisotropy decreases in proportion to $1/M_c^2$. The anisotropies determined from the profiles of figures 2–4 are listed in table 5 and are found to lie below the subsonic level of 0.5. The anisotropies of the M7 and M10 data are almost half that of the M3, confirming that the anisotropy decreases significantly with M_c for the STBLI shear layer although not the extent predicted by the $1/M_c^2$ scaling. The anisotropy at $M_c = 2$ would be approximately 0.083 if calculated by the $1/M_c^2$ law in relation to the anisotropy level of the M3 flow. We note that Forliti *et al.* (2005) found that increasing the strength of the counter-current reverse flow increased $\overline{w'^2}/\overline{u'^2}$ only for $r \leqslant -0.2$.

The reduction in STBLI shear layer anisotropy is primarily due to an increase in the streamwise turbulence component while the cross-stream component increases only slightly. Values for the cross-stream stress of the M3 shear layer are comparable to the

levels experienced in canonical mixing layers near $M_c = 1$. The increase in streamwise turbulence stress from $M_c = 1$ to $M_c = 2$ is opposite to the apparent trends in canonical mixing layer data for which $\overline{u'^2}/\Delta U$ is found to decrease or remain constant with increasing M_c. For example, see the data compilations of Barre & Bonnet (2015) or Pantano & Sarkar (2002) although the data do not extend past $M_c = 1.2$. To make sense of these differences, we turn to the analysis of the turbulent kinetic energy and Reynolds stress budget equations.

The following form of the TKE budget equation is considered:

$$\begin{gathered}
\frac{\partial k}{\partial t} = 0 = \mathcal{C} + \mathcal{P} + \mathcal{T} + \Pi + \epsilon + \Sigma, \\
\mathcal{C} = -\frac{\partial k \tilde{u}_i}{\partial x_i}, \\
\mathcal{P} = -\overline{\rho u_i'' u_j''} \frac{\partial \tilde{u}_i}{\partial x_j}, \\
\mathcal{T} = -\frac{1}{2}\frac{\partial \overline{\rho u_i''^2 u_j''}}{\partial x_j} - \frac{\partial \overline{p' u_i''}}{\partial x_i} + \left(\frac{\partial \overline{u_i'' \sigma_{ij}}}{\partial x_j} + \frac{\partial \overline{u_i'' \tau_{ij}}}{\partial x_j} \right), \\
\Pi = \overline{p' \frac{\partial u_i''}{\partial x_i}}, \\
\epsilon = -\overline{\sigma_{ij} \frac{\partial u_i''}{\partial x_j}} - \overline{\tau_{ij} \frac{\partial u_i''}{\partial x_j}}, \\
\Sigma = -\overline{u_i''} \frac{\partial \bar{p}}{\partial x_i}.
\end{gathered} \tag{5.2}$$

In (5.2), a Reynolds averaged quantity is denoted by an overbar and a fluctuation about the Reynolds average by a single prime such that $u' = u - \bar{u}$. The Favre average is defined as $\tilde{u} = \overline{\rho u}/\bar{\rho}$ and a fluctuation about the Favre average is indicated by the double prime so that $u'' = u - \tilde{u}$. The turbulent kinetic energy is defined as $k = \overline{\rho u_i'' u_i''}/2$. The budget terms are convection $\mathcal{C}$, production $\mathcal{P}$, transport $\mathcal{T}$, pressure strain Π, dissipation ϵ and pressure work Σ. The several terms making up the transport budget are, from left to right, the turbulent diffusion, pressure diffusion and viscous diffusion. The viscous diffusion and viscous dissipation are functions of the fluid shear stress tensor, which is a combination of the LES resolved stress tensor σ_{ij} and the LES subgrid-scale (known as SGS) modelled stress tensor τ_{ij}. The total viscous diffusion in the shear layer is negligible. The subgrid-scale viscous diffusion is calculated as the remainder of the sum of all other terms.

Similarly, the Favre fluctuation Reynolds stress budget equation can be written as the following where $R_{ij} = \overline{\rho u_i'' u_j''}$:

$$\begin{gathered}
\frac{\partial R_{ij}}{\partial t} = 0 = \mathcal{C}_{ij} + \mathcal{P}_{ij} + \mathcal{T}_{ij} + \Pi_{ij} + \epsilon_{ij} + \Sigma_{ij}, \\
\mathcal{C}_{ij} = -\frac{\partial R_{ij} \tilde{u}_k}{\partial x_k},
\end{gathered}$$

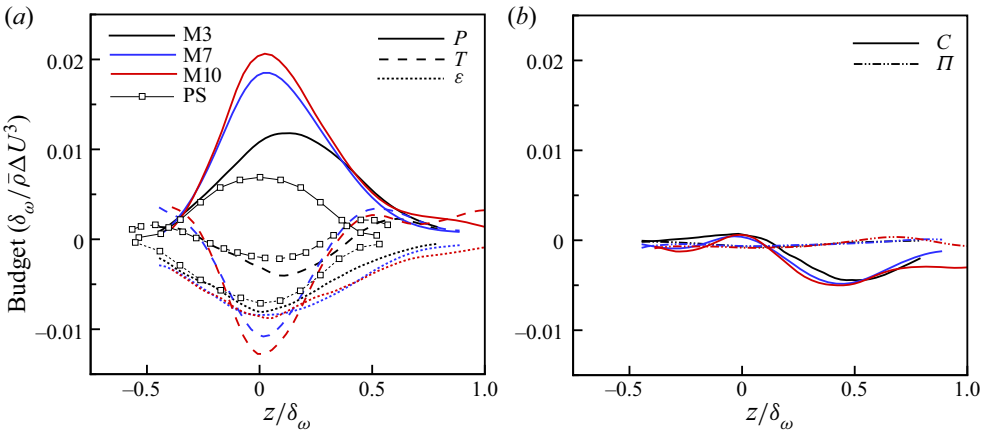

Figure 20. TKE budgets: production, transport and dissipation are plotted in panel (*a*) and convection and pressure strain in panel (*b*). The data of Pantano & Sarkar (2002) is labelled as PS.

$$\mathcal{T}_{ij} = -\frac{\partial \overline{\rho u_i'' u_j'' u_k''}}{\partial x_k} + \frac{\partial \overline{p' u_i''}}{\partial x_j} + \frac{\partial \overline{p' u_j''}}{\partial x_i} + \left(\frac{\partial \overline{\sigma_{jk} u_j''}}{\partial x_k} + \frac{\partial \overline{\sigma_{ik} u_j''}}{\partial x_k} + \frac{\partial \overline{\tau_{jk} u_j''}}{\partial x_k} + \frac{\partial \overline{\tau_{ik} u_j''}}{\partial x_k} \right),$$

$$\Pi_{ij} = \overline{p' \frac{\partial u_i''}{\partial x_j}} + \overline{p' \frac{\partial u_j''}{\partial x_i}}, \tag{5.3}$$

$$\epsilon_{ij} = -\left(\overline{\sigma_{jk} \frac{\partial u_i''}{\partial x_k}} + \overline{\sigma_{ik} \frac{\partial u_j''}{\partial x_k}} \right) - \left(\overline{\tau_{jk} \frac{\partial u_i''}{\partial x_k}} + \overline{\tau_{ik} \frac{\partial u_j''}{\partial x_k}} \right),$$

$$\Sigma_{ij} = -\overline{u_j''} \frac{\partial \bar{p}}{\partial x_i} - \overline{u_i''} \frac{\partial \bar{p}}{\partial x_j}.$$

Pantano & Sarkar (2002) showed in the DNS of temporal mixing layers from $M_c = 0.3$ to 1.1 that the normalized TKE production and transport decreased with increasing M_c while dissipation remained constant. Similar results were obtained by Vreman *et al.* (1996) and by Freund *et al.* (2000). Decreased production resulted in decreased TKE thus reducing turbulence mixing and ultimately the spreading rate. Increasing M_c also has the effect of significantly decreasing the pressure–strain rate components in relation to the incompressible values (Pantano & Sarkar 2002). The pressure–strain terms are primarily responsible for the transfer of turbulence energy from the streamwise direction to the cross-stream direction as it provides the greatest negative (loss) term in R_{11} and the dominant positive (gain) term in the budgets of R_{33} and $-R_{13}$.

The TKE budgets of the three STBLI shear layers are plotted in figure 20 and the Reynolds stress budgets in figure 21. The budget profiles are plotted as functions of $z/\delta_\omega = \zeta/(\mathrm{d}\delta_\omega/\mathrm{d}x)$ and were averaged in the x-direction over the region of approximate similarity defined in § 3.1. All budget terms are nearly symmetric with the exception of the convection profiles which are found to be affected by the proximity of the wall on the low-speed side. The asymmetry of the convection term is responsible for the shift in the turbulence peak noted in § 3.1. The level of convection does not change between the three cases and so its influence in shifting the turbulence peak is greatest for the M3 case with the lowest TKE production. The TKE production and transport increase substantially with increasing Mach number. The same is true for the R_{11} budgets. Production and transport

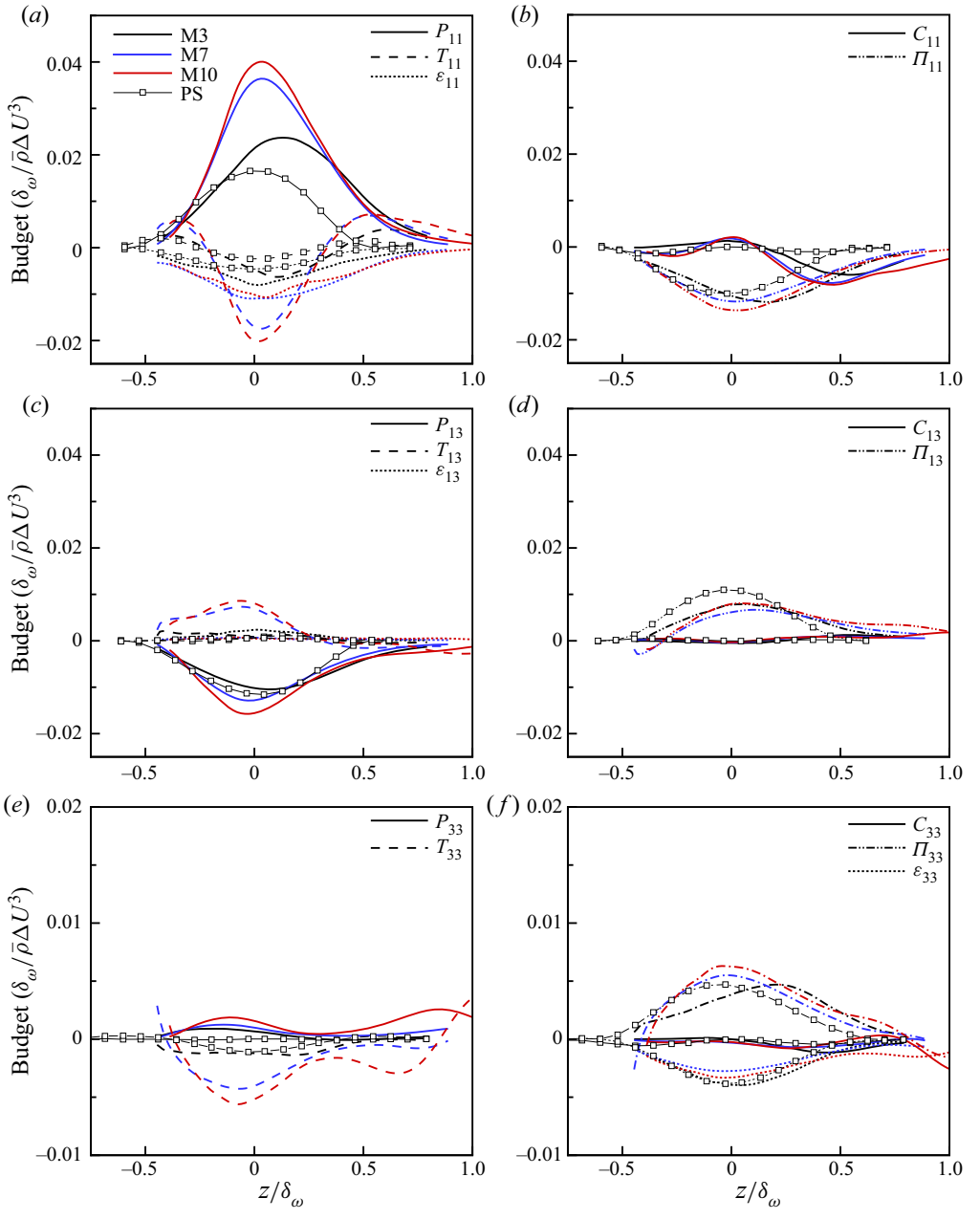

Figure 21. Reynolds stress budgets of R_{11} (*a*,*b*), R_{13} (*c*,*d*) and R_{33} (*e*,*f*). The data of Pantano & Sarkar (2002) is labelled as PS.

are approximately constant across the three cases for R_{33} and increase in magnitude only slightly for R_{13} The observed increase across cases in $\mathcal{T}_{13}$ and $\mathcal{T}_{33}$ is due to an increase in the pressure diffusion. The increase in $\mathcal{T}_{11}$, however, is due entirely to increased turbulence transport as the pressure diffusion remains negligible in all three cases for this budget. Not included in these plots are the pressure work terms Σ and Σ_{ij}, which are negligible for all cases.

Case	Π_{33}/Π_{11}	$\Pi_{11}/\mathcal{P}_{13}$	$\Pi_{33}/\mathcal{P}_{13}$	$\Pi_{13}/\mathcal{P}_{13}$
M3	0.38	1.17	0.45	0.70
M7	0.41	1.12	0.46	0.69
M10	0.40	1.01	0.40	0.74
Freund *et al.* (2000)	0.4	1.0	0.4	0.8

Table 6. Comparison of integrated Reynolds stress pressure–strain budgets.

The data of Pantano & Sarkar (2002) for $M_c = 1.1$ and $s = 1$ are included in figures 20 and 21 for comparison. For this purpose, the data of Pantano & Sarkar were rescaled from the normalization by the mixing layer momentum thickness δ_θ to the vorticity thickness δ_ω. The ratio $\delta_\theta/\delta_\omega$ for this data was obtained by noting that, for a planar mixing layer, $\mathcal{P}\delta_\omega/\bar{\rho}\Delta U^3 = \frac{1}{2}(\mathcal{P}_{11}\delta_\omega/\bar{\rho}\Delta U^3) = -\widetilde{u''w''}/\Delta U^2$. It is obvious that the STBLI shear layers have much higher production and transport rates of TKE and R_{11} than the canonical case. Otherwise, all other budget terms of the M3 shear layer at $M_c = 1$ compare exceptionally well with the data of Pantano & Sarkar, most notably in the pressure–strain terms.

Freund *et al.* (2000) studied the TKE and Reynolds stress budgets for self-similar annular jets at M_c from 0.1 to 1.8 and found that the ratios between the integrated pressure–strain terms (Π_{11}/Π_{33}) and also the ratio of integrated pressure–strain components to turbulent shear stress production ($\Pi_{ij}/\mathcal{P}_{13}$) were nearly constant with M_c. The STBLI Π_{ij} and $\mathcal{P}_{13}$ budget profiles were integrated over z/δ_ω and the various ratios were calculated. These are listed in table 6 and the results are compared with the M_c-independent ratios reported by Freund *et al.* (2000). The closeness between the STBLI shear layer ratios and those of Freund *et al.* indicates that the interchange of turbulence energy is very similar between the two configurations.

From the comparison with the budgets of Pantano & Sarkar and with the ratios of integrated budgets of Freund *et al.*, it is apparent that the most significant difference between the separation shear layer and the canonical case is the greatly increased turbulence production of the separation shear layer. There is more energy in the higher Mach number STBLI flows and therefore more energy is transferred from the mean flow to the turbulence, predominantly through the R_{11} production, but the rate at which the energy is transferred from streamwise to the spanwise component is limited by the pressure–strain rate terms. Both the viscous drain of turbulence energy as well as the transport between the components of turbulence by the pressure strain terms have been shown to be similar to the canonical data suggesting that these properties in the STBLI shear layer are affected by compressibility in the same manner as for the canonical free mixing layer.

6. Conclusions

The present research effectively demonstrates that, even in this assertively non-canonical configuration that is the shear layer in a separated STBLI flow, it is still possible to define a region of approximate mixing-layer-like similarity. Perhaps more surprising is the fact that the STBLI shear layer also shows striking consistency with canonical mixing layer theories as they are currently understood. This fact remains even in the case of the hypersonic separation for which the shear layer high-speed Mach number is above 5 and the temperature ratio across the layer is also above 5.

Concerning the environment in which the shear layers exist, certain factors that prevent this flow from being canonical in nature are the fact that the shear layer is (i) embedded in a turbulent boundary layer; (ii) is subjected to the low-frequency oscillations of the separation shock unsteadiness; (iii) is not aligned with the free stream; and (iv) the low-speed side of the layer is produced by the reverse flow of a shallow separation bubble. In spite of these, we have demonstrated the possibility of obtaining a reasonable collapse of the mean flow profiles and turbulence stress profiles when plotting against a linearly varying similarity variable. This is consistent with a constant spreading rate. The form of the similarity profiles of U and the Reynolds stresses are also reminiscent of canonical mixing layer topology and exhibit the necessary conditions for the Kelvin–Helmholtz instability. Properties of the shear layers were reported, including the estimated conditions of the two streams, the convective Mach number, the estimated linear spreading rates and maximum turbulence stress levels. The peak turbulence shear stress was found to be proportional to the spreading rate by the same relation as for canonical mixing layer data with no dependence on the level of compressibility. Variation of the STBLI shear layer properties with convective Mach number were shown to be consistent with known trends observed in the literature. With respect to the variation of mixing layer properties with increased compressibility as classified by M_c, the data is in the direction of the expected trends. The difference in properties of the M7 and M10 data cases at $M_c = 2$ is consistent with an increase in M_c when compared with M3 at $M_c = 1$. Namely, a decrease in spreading rate with M_c was observed and the extent of this decrease, although not to the level of the classic Langley curve, is consistent with other noted properties of the STBLI shear layers that could also affect the spreading rate, specifically, the elevated reverse flow and the adverse pressure gradient. A decrease in turbulence anisotropy was also observed with increasing M_c. The well-documented increase in three-dimensionality of the vortex rollers with increasing M_c was also shown in the current data. A sophisticated conditional averaging method of the two-point correlations was developed for the purpose of extracting specifically the mixing layer vortex signatures from the turbulent environment. This correlation method also allowed for the direct measurement of the mixing layer convection velocity. Instantaneous visualizations of the vortices showed that the oblique angle of the vortices in the spanwise direction is consistent with predictions by inviscid linear stability theory based on M_c.

It was found through TKE and Reynolds stress budget analysis that the STBLI shear layers have a much greater streamwise turbulence production rate than is observed in the compressible mixing layer data. In spite of this difference, the interchange of turbulence energy among the different turbulence stress components determined from the pressure–strain rate terms was shown to be consistent with mixing layer data at the same M_c. The drain of energy caused by the viscous terms were also consistent. These results indicate that the STBLI shear layer spreading rate, turbulence shear stress and anisotropy are dictated by the same compressible flow phenomena as in the canonical configuration.

Mixing layer conditions that are particularly difficult to set up experimentally occur naturally in the STBLI shear layer: high M_c, high reverse flow, and also an adverse pressure gradient. Although it has its limitations as pointed out above, the STBLI shear layer configuration, as demonstrated by this study, can provide useful data capable of expanding the currently available mixing layer condition parameter space, as well as identifying accurate generalizations of compressible shear layers for the development of turbulence models and scaling laws. In particular, the conservative energy exchange from the streamwise component is less efficient with increasing M_c, thus causing both the spreading rate and the anisotropy to decrease with increasing M_c.

Acknowledgements. This work is supported in part by the Air Force Office of Scientific Research, award number FA9550-17-1-0104 with Dr Leyva, and the Air Force Testing and Evaluation Division, award number FA9550-10-1-0535 with the Center for Testing Excellence at the University of Maryland and the Arnold Engineering Development Center with Dr Marren, Dr Lafferty and Dr Marineau.

Declaration of interests. The authors report no conflict of interest.

Author ORCIDs.
Clara M. Helm http://orcid.org/0000-0002-5527-4194;
M. Pino Martín http://orcid.org/0000-0002-5230-6357;
Owen J.H. Williams http://orcid.org/0000-0002-5470-5028.

References

Aupoix, B. 2004 Modeling of compressibility effects in mixing layers. *J. Turbul.* **5**, N7.

Aupoix, B. & Bézard, H. 2006 Compressible mixing layers: data analysis and modeling. *ERCOFTAC Bull.* **70**, 13–17.

Bardina, J., Ferziger, J.H. & Reynolds, W.C. 1980 Improved subgrid-scale models for large eddy simulation. *AIAA Paper* 1980-1357.

Barone, M.F., Oberkampf, W.L. & Blottner, F.G. 2006 Validation case study: prediction of compressible turbulent mixing layer growth rate. *AIAA J.* **44** (7), 1488–1497.

Barre, S. & Bonnet, J.-P. 2015 Detailed experimental study of a highly compressible supersonic turbulent plane mixing layer and comparison with most recent dns results: 'towards an accurate description of compressibility effects in supersonic free shear flows'. *Intl J. Heat Fluid Flow* **51**, 324–334.

Barre, S., Quine, C. & Dussauge, J.P. 1994 Compressibility effects on the structure of supersonic mixing layers: experimental results. *J. Fluid Mech.* **259**, 47–78.

Birch, S.F. & Eggers, J.M. 1972 Free turbulent shear flows. *NASA Tech. Rep.* SP-321. National Aeronautics and Space Administration.

Bogdanoff, D.W. 1983 Compressibility effects in turbulent shear layers. *AIAA J.* **21** (6), 926–927.

Breidenthal, R.E. 1992 Sonic eddy–a model for compressible turbulence. *AIAA J.* **30** (1), 101–104.

Brown, G.L. & Roshko, A. 1974 On the density effects and large structures in turbulent mixing layers. *J. Fluid Mech.* **64**, 775–781.

Brown, G.L. & Thomas, A.S.W. 1977 Large structure in a turbulent boundary layer. *Phys. Fluids* **20** (10), S243–S252.

Channapragada, R.S. 1963 Compressible jet spread parameter for mixing zone analyses. *AIAA J.* **1** (9), 2188–2190.

Cherry, N.J., Hillier, R. & Latour, M.E.M.P. 1984 Unsteady measurements in a separated and reattaching flow. *J. Fluid Mech.* **144**, 13–46.

Chinzei, N., Masuya, G., Komuro, T., Murakami, A. & Kudou, K. 1986 Spreading of two-stream supersonic turbulent mixing layers. *Phys. Fluids* **29**, 1345–1347.

Clemens, N.T. & Mungal, M.G. 1992 Two- and three-dimensional effects in the supersonic mixing layer. *AIAA J.* **30** (4), 973–981.

Clemens, N.T. & Mungal, M.G. 1995 Large-scale structure and entrainment in the supersonic mixing layer. *J. Fluid Mech.* **284**, 171–216.

Day, M.J., Reynolds, W.C. & Mansour, N.N. 1998 The structure of the compressible reacting mixing layer: insights from linear stability analysis. *Phys. Fluids* **10** (4), 993–1007.

Debisschop, J.-R., Chambres, O. & Bonnet, J.-P. 1994 Velocity field characteristics in supersonic mixing layers. *J. Expl Therm. Fluid Sci.* **9**, 147–155.

Dimotakis, P.E. 1991 Turbulent free shear layer mixing and combustion. In *High-Speed Flight Propulsion Systems* (ed. E.T. Curran & S.N.B Murthy), vol. 137, chap. 5, pp. 265–340. AIAA.

Dupont, P., Haddad, C. & Debiève, J.F. 2006 Space and time organization in a shock-induced separated boundary layer. *J. Fluid Mech.* **559**, 255–277.

Dupont, P., Muscat, P. & Dussauge, J.-P. 1999 Localisation of large scale structures in a supersonic mixing layer: a new method and first analysis. *Flow Turbul. Combust.* **62**, 335–358.

Dupont, P., Piponniau, S. & Dussauge, J.P. 2019 Compressible mixing layer in shock-induced separation. *J. Fluid Mech.* **863**, 620–643.

Dupont, P., Piponniau, S., Sidorenko, A. & Debiève, J.F. 2008 Investigation by particle image velocimetry measurements of oblique shock reflection with separation. *AIAA J.* **46** (6), 1365–1370.

DUSSAUGE, J.P., DUPONT, P. & DEBIÈVE, J.F. 2006 Unsteadiness in shock wave boundary layer interaction with separation. *Aerosp. Sci. Technol.* **10**, 85–91.

ELLIOTT, G.S. & SAMIMY, M. 1990 Compressibility effects in free shear layers. *Phys. Fluids* A **2**, 1231–1240.

FORLITI, D.J., TANG, A.B. & STRYKOWSKI, P.J. 2005 An experimental investigation of planar countercurrent turbulent shear layers. *J. Fluid Mech.* **530**, 479–486.

FREUND, J.B., LELE, S.K. & MOIN, P. 2000 Compressibility effects in a turbulent annular mixing layer. Part 1. Turbulence and growth rate. *J. Fluid Mech.* **421**, 229–267.

GATSKI, T.B. & BONNET, J.-P. 2013 *Compressibility, Turbulence and High Speed Flow*, pp. 169–229. Elsevier.

GOEBEL, S.G. & DUTTON, J.C. 1991 Experimental study of compressible turbulent mixing layers. *AIAA J.* **29** (4), 538–546.

GRAFTIEAUX, L., MICHARD, M. & GROSJEAN, N. 2001 Combining PIV, POD and vortex identification algorithms for the study of unsteady turbulent swirling flows. *Meas. Sci. Technol.* **12**, 1422–1429.

GRUBER, M.R., MESSERSMITH, N.L. & DUTTON, J.C. 1993 Three-dimensional velocity field in a compressible mixing layer. *AIAA J.* **31** (11), 2061–2067.

HELM, C. & MARTIN, M.P. 2015 Preliminary LES of hypersonic shock/turbulent boundary layer interactions. *AIAA Paper* 2015-1064.

HELM, C. & MARTIN, M.P. 2016 New LES of a hypersonic shock/turbulent boundary layer interaction. *AIAA Paper* 2016-0346.

HELM, C.M. & MARTÍN, M.P. 2020 Large eddy simulation of two separated hypersonic shock/turbulent boundary layer interactions. *Phys. Rev. Fluids* (in preparation for submission).

HUERRE, P. & MONKEWITZ, P.A. 1985 Absolute and convective instabilities in free shear layers. *J. Fluid Mech.* **159**, 151–168.

IKAWA, H. & KUBOTA, T. 1975 Investigation of supersonic turbulent mixing layer with zero pressure gradient. *AIAA J.* **13** (5), 566–572.

JACKSON, T.L. & GROSCH, C.E. 1990 Absolute/convective instabilities and the convective mach number in a compressible mixing layer. *Phys. Fluids* A **2**, 949.

KIYA, M. & SASAKI, K. 1983 Structure of a turbulent separation bubble. *J. Fluid Mech.* **137**, 83–113.

KLINE, S.J., CANTWELL, B.J. & LILLEY, G.M. 1980 In *Proceedings 1980 Conference on Complex Turbulent Flows, Vol. I*, pp. 364–366. Stanford University.

KÖNIG, O., SCHULÜLTER, J. & FIEDLER, H.E. 1998 Turbulent mixing layer in adverse pressure gradient. *Progress in Fluid Flow Research: Turbulence and Applied MHD*, pp. 15–29.

KORST, H.H. & TRIPP, W. 1957 The pressure on a blunt trailing edge separating two-supersonic two-dimensional air streams of different mach numbers and stagnation pressures but identical stagnation temperatures. In *Fifth Midwestern Conference on Fluid Mechanics, Ann Arbor, Michigan*. University of Michigan Press.

KOURTA, A. & SAUVAGE, R. 2002 Computaion of supersonic mixing layers. *Phys. Fluids* **14** (11), 3790–3797.

LELE, S.K. 1989 Direct numerical simulation of compressible free shear flows. *AIAA Paper* 89-0374.

LELE, S.K. 1994 Compressibility effects on turbulence. *Annu. Rev. Fluid Mech.* **26**, 211–54.

LESIEUR, M. 1987 In *Turbulence in Fluids, Dordrecht, The Netherlands*. Marinus Nijhoff Publishers.

LIN, C.C. 1953 *NACA Tech. Note* 2887.

MARTÍN, M.P. 2000 Shock capturing and the LES of high-speed flows. In *Annual Research Briefs*. Center for Turbulence Research, NASA Ames/Stanford University.

MARTÍN, M.P., PIOMELLI, U. & CANDLER, G.V. 2000 Subgrid-scale models for compressible large-eddy simulations. *Theor. Comput. Fluid Dyn.* **13** (3), 361–376.

MARTÍN, M.P., TAYLOR, E.M., WU, M. & WEIRS, V.G. 2006 A bandwidth-optimized weno scheme for the direct numerical simulation of compressible turbulence. *J. Comput. Phys.* **220** (1), 270–289.

MEHTA, R.D. & WESTPHAL, R.V. 1984 Near-field turbulence properties of single- and two-stream plane mixing layers. *AIAA Paper* 1984-0426.

MILES, J.W. 1959 The stability of a shear layer in an unbounded heterogenous inviscid fluid. *J. Fluid Mech.* **6**, 538–522.

PAI, S.I. 1955 On turbulent jet mixing of two gases at constant temperature. *J. Appl. Mech.* **22**, 41–47.

PANTANO, C. & SARKAR, S. 2002 A study of compressibility effects in the high-speed turbulent shear layer using direct numerical simulation. *J. Fluid Mech.* **451**, 329–371.

PAPAMOSCHO, D. & ROSHKO, A. 1988 The compressible turbulent shear layer: an experimental study. *J. Fluid Mech.* **197**, 453–477.

PAPAMOSCHOU, D. 1995 Evidence of shocklets in a counterflow supersonic shear layer. *Phys. Fluids* **7**, 233–235.

PAVITHRAN, S. & REDEKOPP, L.G. 1989 The absolute-convective transition in subsonic mixing layers. *Phys. Fluids* A **1**, 1736–1739.

PIPONNIAU, S., DUSSAUGE, J.P., DEBIÈVE, J.F & DUPONT, P. 2009 A simple model for low-frequency unsteadiness in shock-induced separation. *J. Fluid Mech.* **629**, 87–108.

PRIEBE, S. & MARTÍN, M.P. 2012 Low-frequency unsteadiness in shock wave-turbulent boundary layer interaction. *J. Fluid Mech.* **699**, 1–49.

PRIEBE, S. & MARTÍN, M.P. 2020 Turbulence in a hypersonic ramp flow. *Phys. Rev. Fluids* (accepted for publication).

ROSSMANN, T., MUNGAL, M.G. & HANSON, R.K. 2002 Evolution and growth of large-scale structures in high compressibility mixing layers. *J. Turbul.* **3**, N9.

SAMIMY, M. & ELLIOTT, G.S. 1990 Effects of compressibility on the characteristics of free shear flow. *AIAA J.* **28** (3), 439–445.

SAMIMY, M., REEDER, M.F. & ELLIOTT, G.S. 1992 Compressibility effects on large structures in free shear flows. *Phys. Fluids* A **4** (6), 1251–1258.

SANDHAM, N.D. & REYNOLDS, W.C. 1990 Compressible mixing layer: linear theory and direct simulation. *AIAA J.* **28** (4), 618–624.

SANDHAM, N.D. & REYNOLDS, W.C. 1991 Thee-dimensional simulation of large eddies in the compressible mixing layer. *J. Fluid Mech.* **224**, 133–158.

SLESSOR, M.D., ZHUANG, M. & DIMOTAKIS, P.E. 2000 Turbulent shear-layer mixing; growth-rate compressibility scaling. *J. Fluid Mech.* **414**, 35–45.

SMITS, A.J. & DUSSAUGE, J.P. 2006 *Turbulent Shear Layers in Supersonic Flow*, 2nd edn. Springer.

STRYKOWSKI, P.J., KROTHAPALLI, A. & JENDOUBI, S. 1996 The effect of counterflow on the development of compressible shear layers. *J. Fluid Mech.* **308**, 63–96.

TAYLOR, E.M. & MARTÍN, M.P. 2007 Stencil adaption properties of a weno scheme in direct numerical simulations of compressible turbulence. *J. Sci. Comput.* **30**, 533–554.

TAYLOR, E.M. & MARTÍN, M.P. 2008 Synchronization of weighted essentially non-oscillatory methods. *Communications in Comp. Phy.* **4** (1), 56–71.

TAYLOR, E.M., WU, M. & MARTÍN, M.P. 2007 Optimization of nonlinear error for weighted non-oscillatory methods in direct numerical simulations of compressible turbulence. *J. Comput. Phys.* **22**, 384–297.

TENNEKES, H. & LUMLEY, J.L. 1972 *A First Course in Turbulence*. The MIT Press.

THUROW, B.S., JIANG, N., KIM, J.-W., LEMPERT, W. & SAMIMY, M. 2008 Issues with measurements of convective velocity of large-scale structures in the compressible shear layer of a free jet. *Phys. Fluids* **20**, 066101.

TRICHILO, J., HELM, C. & MARTIN, M.P. 2019 Persistence of a centrifugal instability in shock-separated flows at Mach 3 through 10. *AIAA Paper* 2019-1130.

VREMAN, A.W., SANDHAM, N.D. & LUO, K.H. 1996 Compressible mixing layer growth rate and turbulence characteristics. *J. Fluid Mech.* **320**, 235–258.

WHITE, F.M. 1974 *Viscous Fluid Flow*. McGraw–Hill.

WU, M. & MARTÍN, M.P. 2007 Direct numerical simulation of supersonic turbulent boundary layer over a compression ramp. *AIAA J.* **45** (4), 879–889.

WU, M. & MARTÍN, M.P 2008 Analysis of shock motion in shockwave and turbulent boundary layer interaction using direct numerical simulation data. *J. Fluid Mech.* **594**, 71–83.